CHAPTER 7

EFFECT OF MOV ARRESTER AND CIRCUIT PARAMETERS ON THE ISOLATED SUBHARMONIC SOLUTIONS

7.1 INTRODUCTION

Metal oxide varistor (MOV) arresters are ubiquitous and have almost replaced the conventional gapped silicon carbide arresters in the distribution environment. Significant advantages of MOV arresters over SiC arresters include superior protective characteristics, improved reliability, superior performance on low impedance circuits and superior energy absorbing capability. The MOV arrester conducts continuously and will conduct even more as the steady state system voltage is raised. Hence, the MOV arresters are exposed to system overvoltage conditions caused by ferroresonance. This necessitates the analysis of the global dynamic behaviour exhibited by the system protected by MOV arrester during ferroresonant condition. This chapter reports investigations carried out to analyse the effect of metal oxide arrester on the isolated subharmonics that occur during ferroresonance. The presence of MOV arrester may affect occurrence and magnitude of the subharmonic ferroresonant oscillations. It is known that the arresters may in some cases cause ferroresonance “dropout” (Walling et al 1994). The investigations reported in this chapter also address the effect of core loss, transformer saturation and source capacitance on the isolated subharmonic solutions.

The initial subharmonic steady states are obtained from temporal bifurcation diagrams. Locally parameterised continuation algorithm is used for tracing the continuum of isolated subharmonic solutions. The hybrid bifurcation

diagrams are used to unearth the solutions hidden in subharmonic flip segments. Analysis reveals the occurrence of higher order banded chaotic solutions, namely, 9-band, 11-band and 21-band. Time domain simulation has been carried out using fourth order Runge-Kutta method and results corroborated using MicroTran. Phase plots, conventional and evolving Poincaré maps are used to identify periodic and chaotic motions.

7.2 SYSTEM DESCRIPTION AND COMPONENT MODELLING

The system under investigation is same as the one considered in Chapter 5 but with the MOV arrester connected across the transformer winding. The three phase circuit of the system is shown in Fig.7.1. Fig.7.2 shows the Thévenin equivalent of the system when viewed between terminals 2c and n. The transformer saturation characteristic is modelled by a two-term polynomial of flux linkage. The core loss is modelled by a linear resistor (R_m). The system parameter values considered for investigation are in p.u. and are given in Appendix 1.

7.2.1 Arrester characteristics

Arrester is modelled as per H. W. Dommel and I. I. Dommel (1978):

$$i_{AR} = f(v_{Lm})$$
$$= (|v_{Lm}| / k)^{\alpha} \text{ sign of } v_{Lm} \quad (7.1)$$

where,

i_{AR} is the arrester current.

v_{Lm} is the voltage across the transformer.

The arrester characteristics for different values of k and α are shown in Fig.7.3. The parameter k is the arrester knee voltage, which determines the voltage magnitude at which conduction commences and parameter α influences the

magnitude of current during conduction. The above model of the arrester is considered adequate for ferroresonance studies (A. Bayadi et al 2003).

7.2.2 Formulation of the state space equations

The state space equations that describe the dynamics of the ferroresonant circuit, Fig.7.2, are derived by the topological approach.
The chosen state variables are:

$$x_1 = v_C \; ; \; x_2 = \phi_{Lm}$$

where,

v_C is the voltage across the capacitor.

ϕ_{Lm} is the transformer flux linkage.

The dynamics of this circuit can be described by the following system of nonlinear differential equations:

$$\boldsymbol{p}x_1 = \{ - x_1 + R_m (a\, x_2 + b\, x_2^{\,q}) + E_{Th} \sin(\omega t) \} / C_{Th} R_m + i_{AR} \qquad (7.2a)$$

$$\boldsymbol{p}x_2 = E_{Th} \sin(\omega t) - x_1 = v_{Lm} \qquad (7.2b)$$

where,

q is the degree of transformer saturation characteristic = 7,11.

a, b are the coefficients of nonlinear function which represent magnetisation characteristic.

v_{Lm} is the voltage across the transformer.

R_m is the transformer core loss.

C_{Th} is the source capacitance.

$\boldsymbol{p}$ is the time derivative operator.

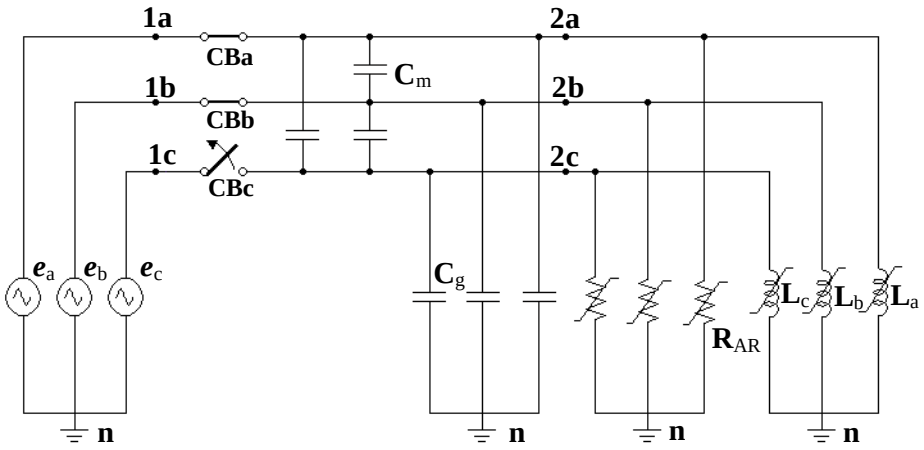

Fig.7.1 A three phase circuit diagram of a cable–fed unloaded transformer connected with arrester.

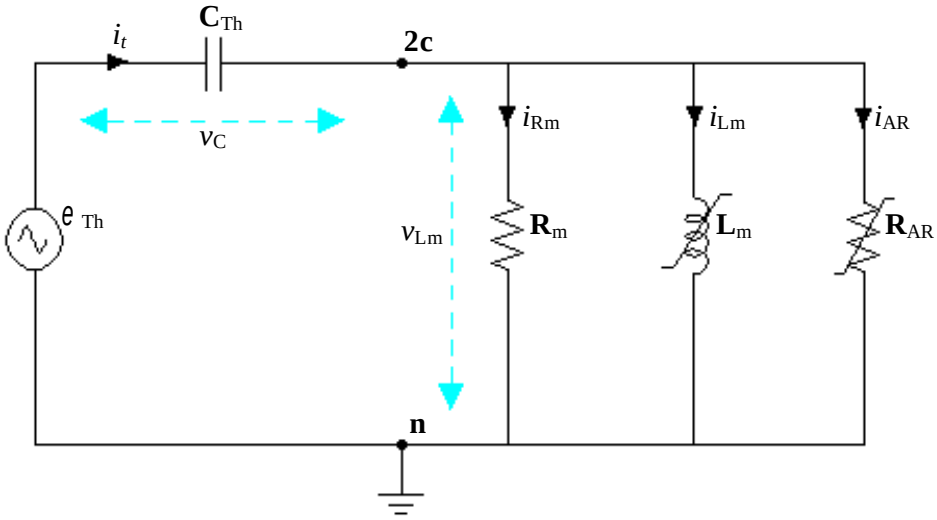

Fig.7.2 Basic ferroresonance circuit for single phase open configuration with arrester connected across transformer.

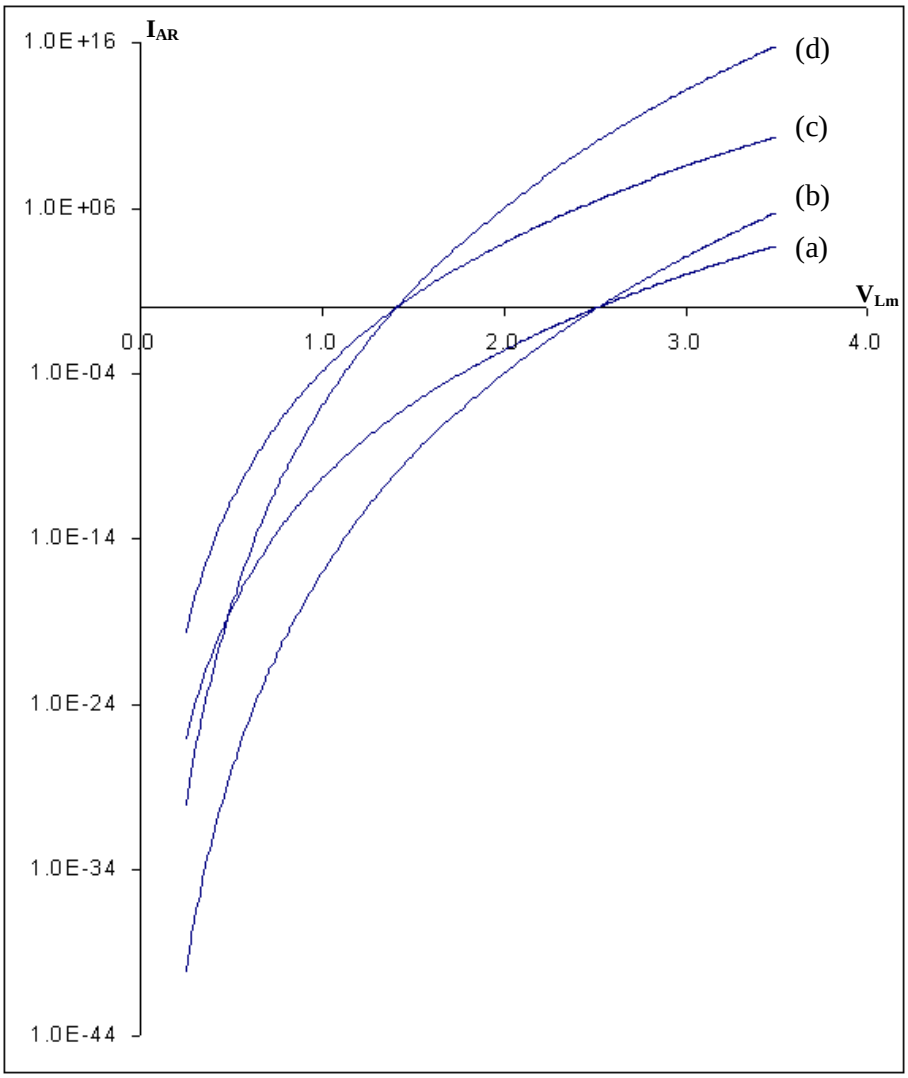

Fig.7.3 Arrester characteristics for different values of k and α.

(a) k = 2.51, α = 26.
(b) k = 2.51, α = 40.
(c) k = 1.41, α = 26.
(d) k = 1.41, α = 40.

7.2.3 Time domain simulation and validation

Equations (7.2a) and (7.2b) are integrated using fourth order Runge-Kutta method. Figures 7.4 and 7.5 show the time domain responses obtained from MicroTran and fourth order Runge-Kutta method (RK4) respectively. As can be seen, the results match perfectly.

7.3 TEMPORAL BIFURCATION DIAGRAM

Temporal bifurcation diagrams have been generated for several cases with various combination of i) transformer core loss ii) transformer saturation index iii) source capacitance iv) presence of arrester. The cases considered for investigations are summarised in case matrices shown in Tables 7.1 to 7.4. The periodicity of solutions obtained for the cases considered are presented in Tables 7.5 to 7.8. The relevant temporal bifurcation diagrams are shown in Figures 7.6 to 7.10. It can be observed from Figures 7.6a and 7.6b that arrester is effective in reducing the number of subharmonic solutions for lower transformer core saturation. Figure 7.7a and 7.7b confirm the same.

Higher order subharmonic solutions viz. period 11, period 15 and period 21 are obtained in both with and without arrester cases. It is to be noted that existence of higher order subharmonic solutions are most likely in lower core loss cases. Figures 7.11a to 7.11f show the phase plots and conventional Poincaré maps of higher order subharmonic solutions. It can be seen from the figures that all the odd subharmonics possess symmetry. The time domain plots of period 15 oscillation for 30 cycles of source (i.e. 2 cycles of period 15 solution) are shown in Fig.7.12a and Fig.7.12b. The Fourier spectrum of the same is shown in Fig.7.13. As expected, the peaks correspond to odd multiples of the base frequency (4 Hz).

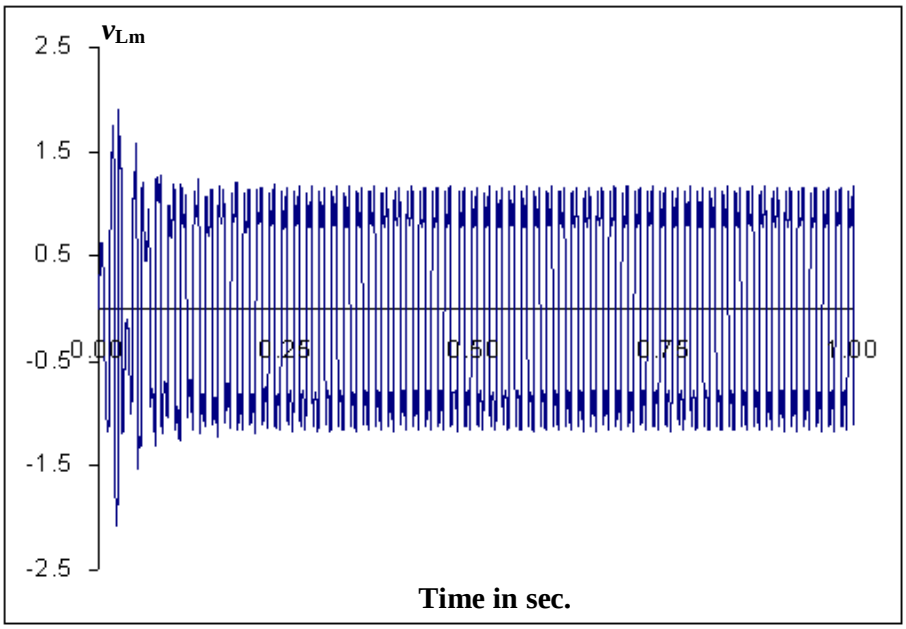

Fig.7.4 Time plot of the voltage across the transformer (v_{Lm}) in Figure 7.2 from MicroTran: E_{Th} = 0.70 p.u., q = 11, C_{Th} = 0.047, R_m = 300, with arrester. Initial condition: $\phi_{Lm}(0) = 0$, $v_C(0) = 0$.

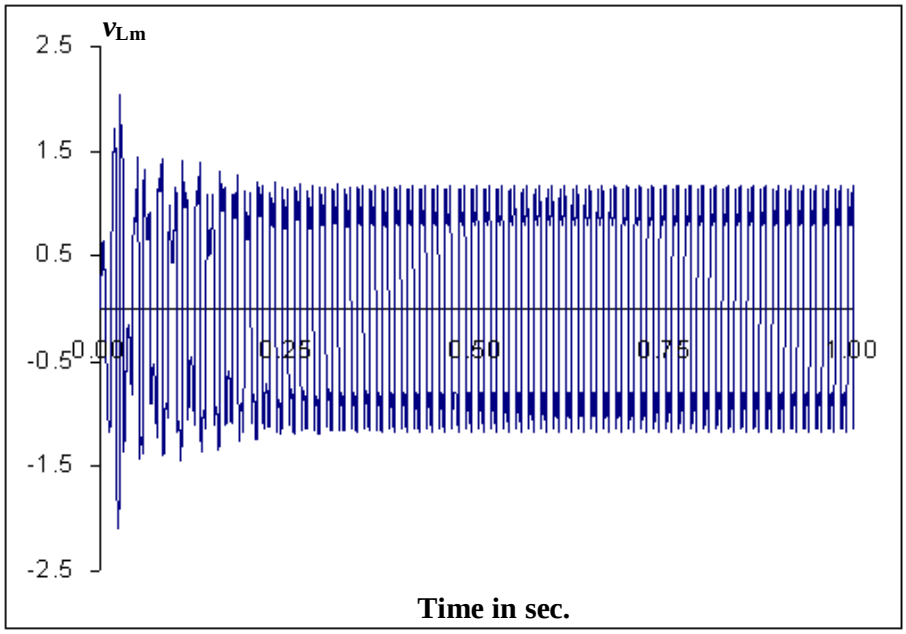

Fig.7.5 Time plot of the voltage across the transformer (v_{Lm}) in Figure 7.2 from RK4 method: E_{Th} = 0.70 p.u., q = 11, R_m = 300, C_{Th} = 0.047, with arrester. Initial condition: $x_1(0) = 0$, $x_2(0) = 0$.

Table 7.1 Case matrix A.1: Without arrester, C_{Th} = 0.0616 p.u.

q/R_m	300 p.u.	600 p.u.
7	A.1.1	A.1.2
11	A.1.3	A.1.4

Table 7.2 Case matrix B.1: Without arrester, C_{Th} = 0.047 p.u.

q/R_m	300 p.u.	600 p.u.
7	B.1.1	B.1.2
11	B.1.3	B.1.4

Table 7.3 Case matrix C.1: With arrester, C_{Th} = 0.0616 p.u.

q/R_m	300 p.u.	600 p.u.
7	C.1.1	C.1.2
11	C.1.3	C.1.4

Table 7.4 Case matrix D.1: With arrester, C_{Th} = 0.047 p.u.

q/R_m	300 p.u.	600 p.u.
7	D.1.1	D.1.2
11	D.1.3	D.1.4

Table 7.5 Periodicity of solutions obtained for Case matrix A.1.

q/R_m	300 p.u.	600 p.u.
7	P_1, P_2, P_3, P_5, P_7 and P_9 Fig.7.6a	P_1, P_2, P_3, P_5, P_7, P_9 and P_{21} Fig.7.7a
11	P_1, P_2, P_3, P_5, P_7 and P_9 Fig.7.8a	P_1, P_2, P_3, P_5 and P_9 Fig.7.9a

Table 7.6 Periodicity of solutions obtained for Case matrix B.1.

q/R_m	300 p.u.	600 p.u.
7	P_1, P_2, P_3 and P_9 Fig.5.7a (Chapter 5)	P_1, P_2, P_3, P_5, P_7 and P_9 Fig.5.7b (Chapter 5)
11	P_1, P_2, P_3, P_5 and P_9 Fig.5.7c (Chapter 5)	P_1, P_2, P_3, P_5 and P_9 Fig.5.7d (Chapter 5)

Table 7.7 Periodicity of solutions obtained for Case matrix C.1.

q/R_m	300 p.u.	600 p.u.
7	P_1 and P_3 Fig.7.6b	P_1, P_2 and P_3 Fig.7.7b
11	P_1, P_2, P_3, P_5, P_7 and P_9 Fig.7.8b	P_1, P_2, P_3, P_5, P_7, P_9, P_{11} and P_{15} Fig.7.9b

Table 7.8 Periodicity of solutions obtained for Case matrix D.1.

q/R_m	300 p.u.	600 p.u.
7	P_1, P_3 and P_9 Fig.7.10a	P_1, P_2 and P_3 Fig.7.10b
11	P_1, P_2, P_3, P_5, P_9 and P_{15} Fig.7.10c	P_1, P_2, P_3, P_5, P_7, P_9 and P_{11} Fig.7.10d

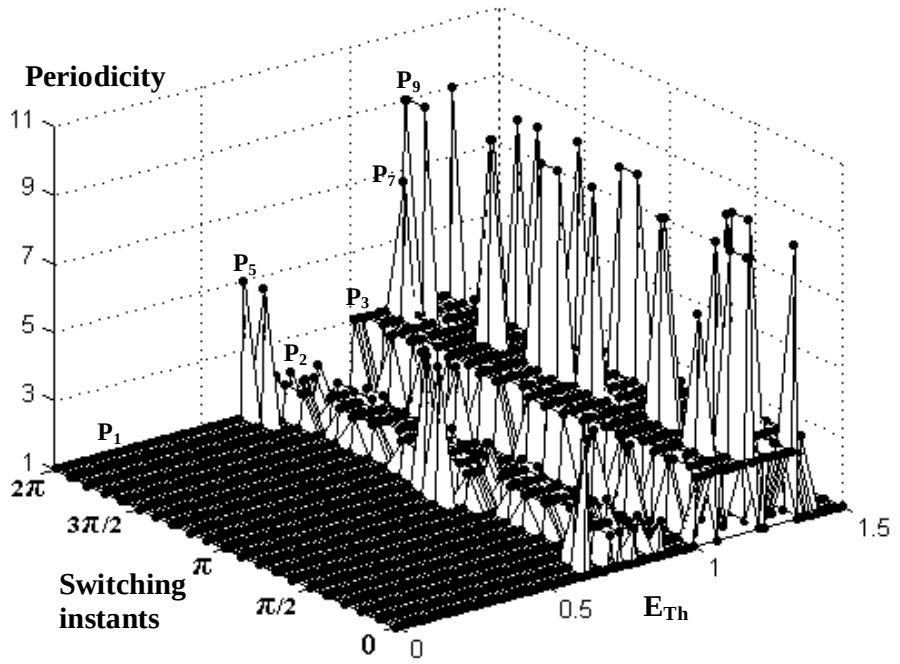

Fig.7.6a Temporal bifurcation diagram for Case A.1.1. (q = 7, R_m = 300, without arrester, C_{Th} = 0.0616). P_1 – fundamental solution, P_2, P_3, P_5, P_7 and P_9 – isolated subharmonic solutions.

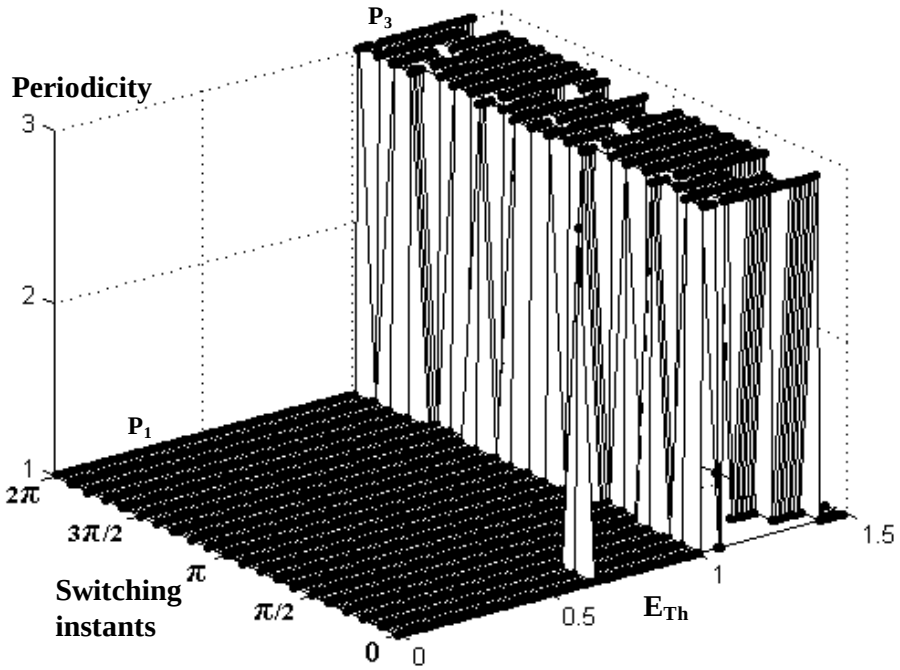

Fig.7.6b Temporal bifurcation diagram for Case C.1.1. (q = 7, R_m = 300, with arrester, C_{Th} = 0.0616).
P_1 – fundamental solution, P_3 – isolated subharmonic solution.

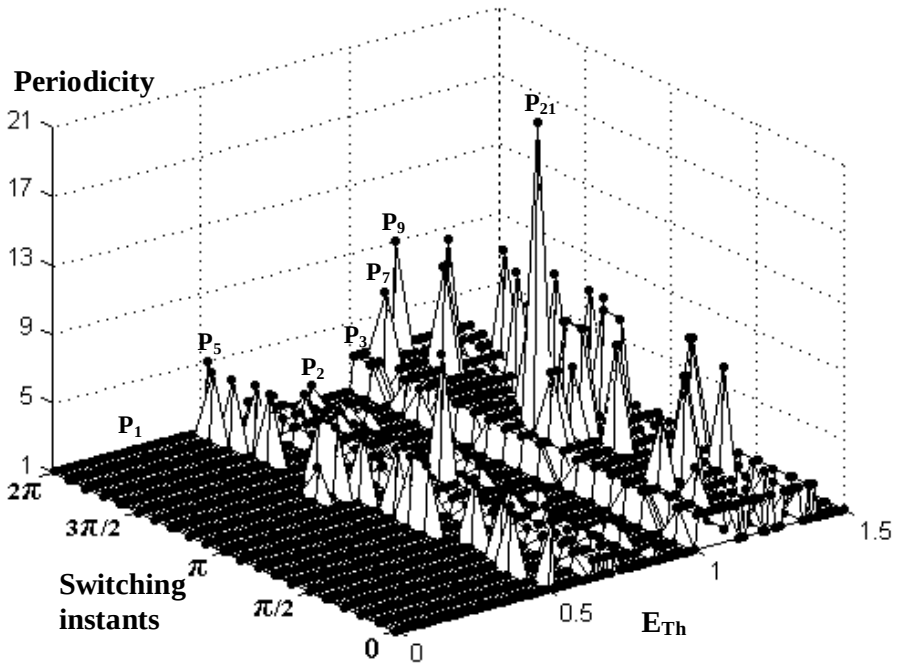

Fig.7.7a Temporal bifurcation diagram for Case A.1.2. (q = 7, R_m = 600, without arrester, C_{Th} = 0.0616).
P_1 – fundamental solution, P_2, P_3, P_5, P_7, P_9 and P_{21} – isolated subharmonic solutions.

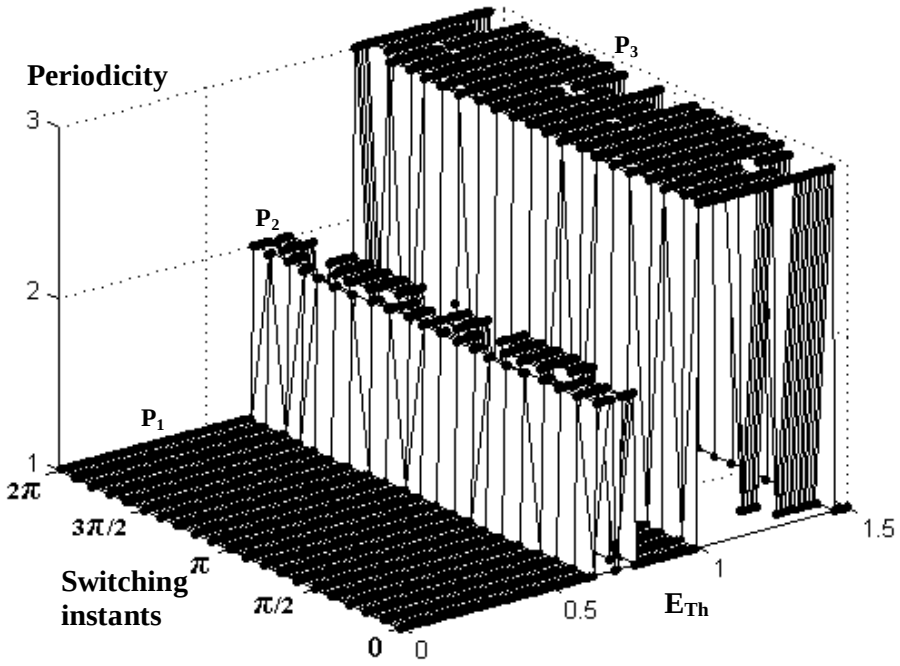

Fig.7.7b Temporal bifurcation diagram for Case C.1.2. (q = 7, R_m = 600, with arrester, C_{Th} = 0.0616).
P_1 – fundamental solution, P_2 and P_3 – isolated subharmonic solutions.

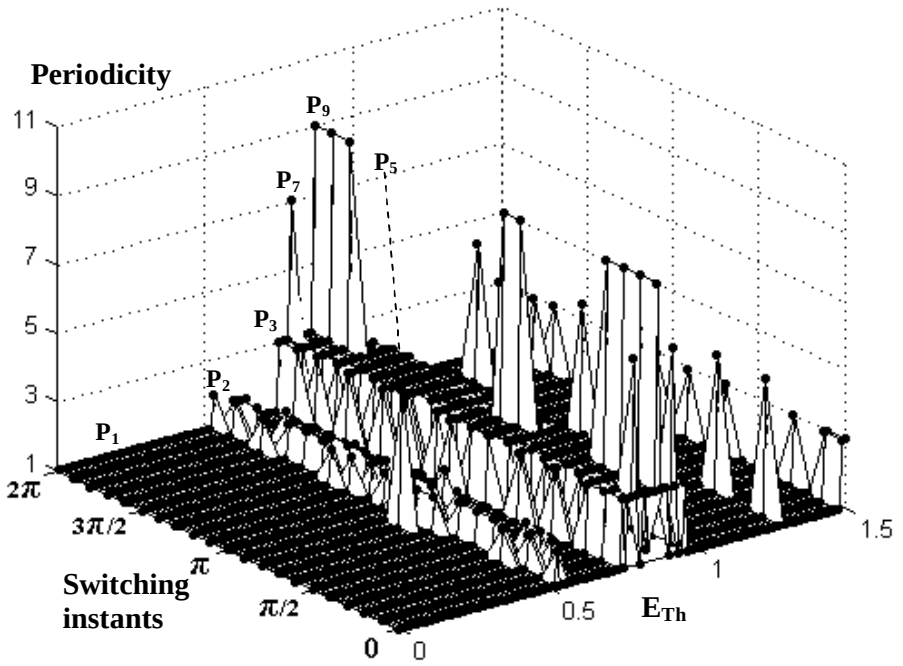

Fig.7.8a Temporal bifurcation diagram for Case A.1.3. (q = 11, R_m = 300, without arrester, C_{Th} = 0.0616).
P_1 – fundamental solution, P_2, P_3, P_5, P_7 and P_9 – isolated subharmonic solutions.

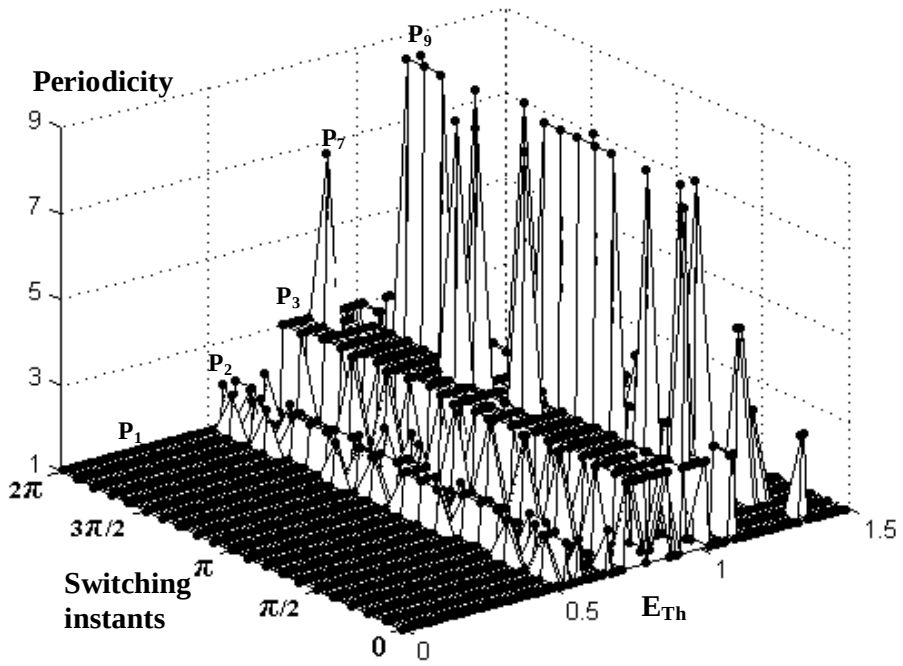

Fig.7.8b Temporal bifurcation diagram for Case C.1.3. (q = 11, R_m = 300, with arrester, C_{Th} = 0.0616).
P_1 – fundamental solution, P_2, P_3, P_5, P_7, and P_9 – isolated subharmonic solutions.

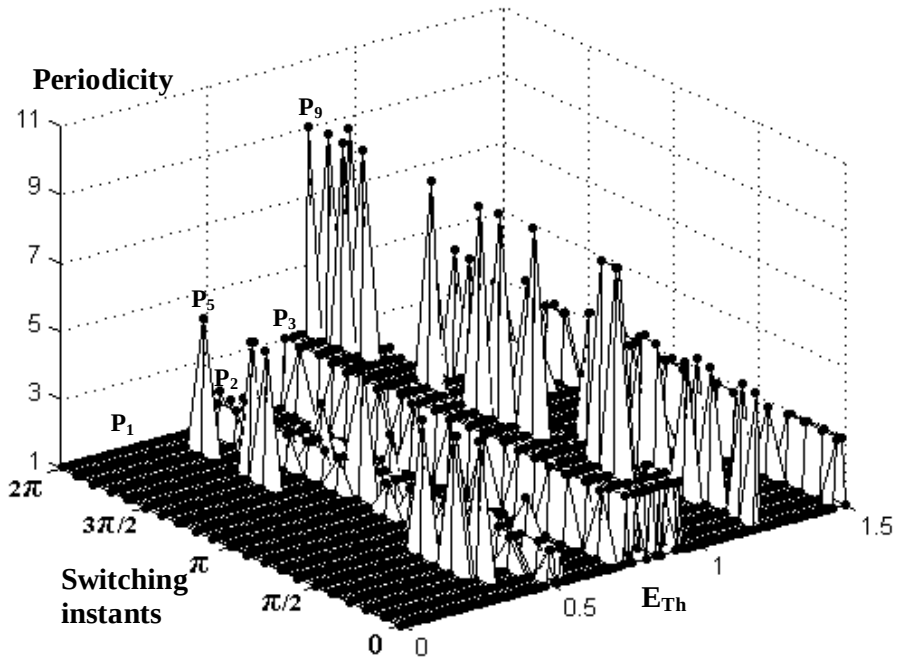

Fig.7.9a Temporal bifurcation diagram for Case A.1.4. (q = 11, R_m = 600, without arrester, C_{Th} = 0.0616).
P_1 – fundamental solution, P_2, P_3, P_5 and P_9 – isolated subharmonic solutions.

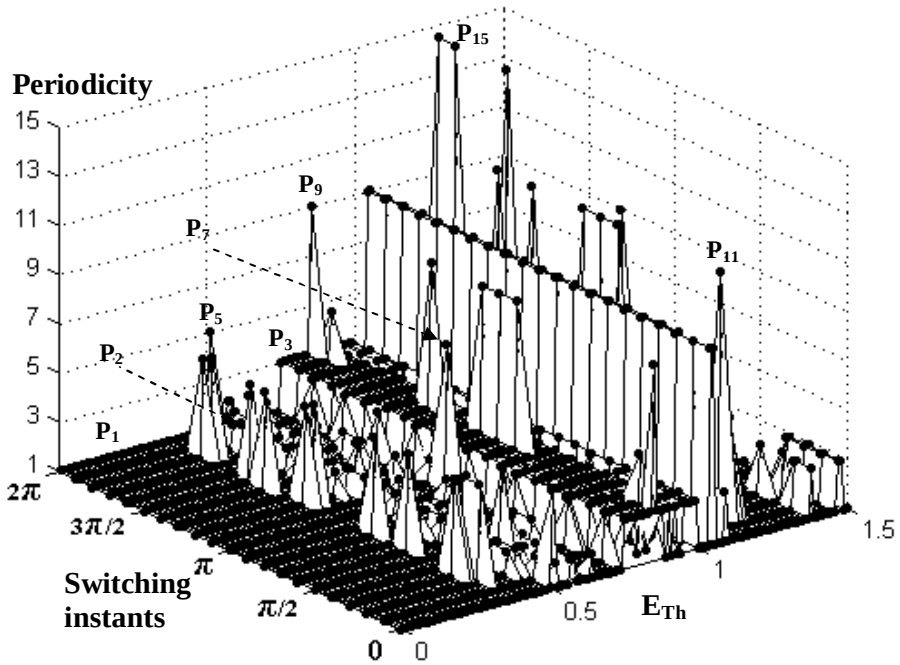

Fig.7.9b Temporal bifurcation diagram for Case C.1.4. (q = 11, R_m = 600, with arrester, C_{Th} = 0.0616).
P_1 – fundamental solution, P_2, P_3, P_5, P_7, P_9, P_{11} and P_{15} – isolated subharmonic solutions.

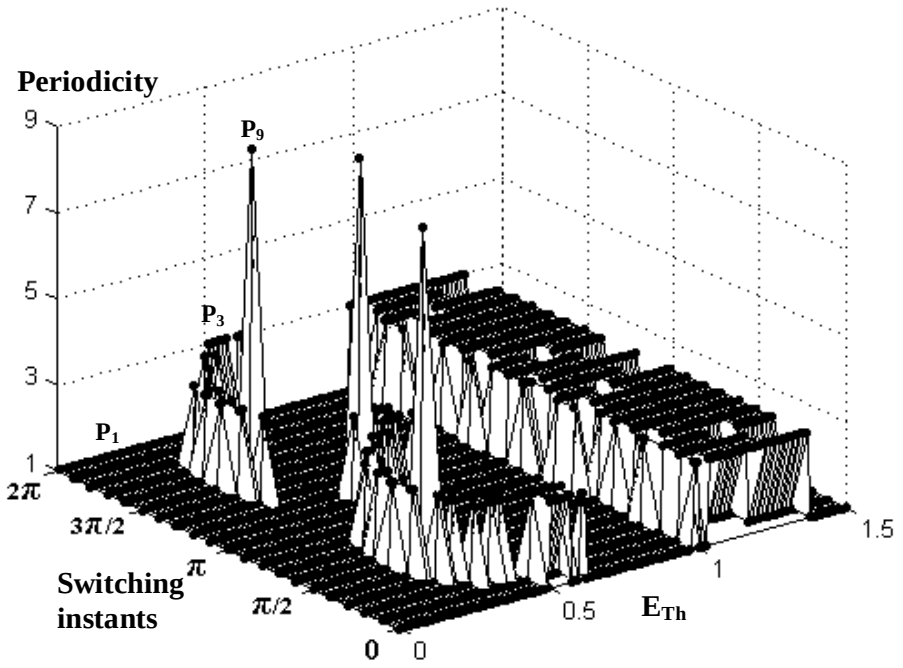

Fig.7.10a Temporal bifurcation diagram for Case D.1.1. (q = 7, R_m = 300, with arrester, C_{Th} = 0.047).
P_1 – fundamental solution, P_3 and P_9 – isolated subharmonic solutions.

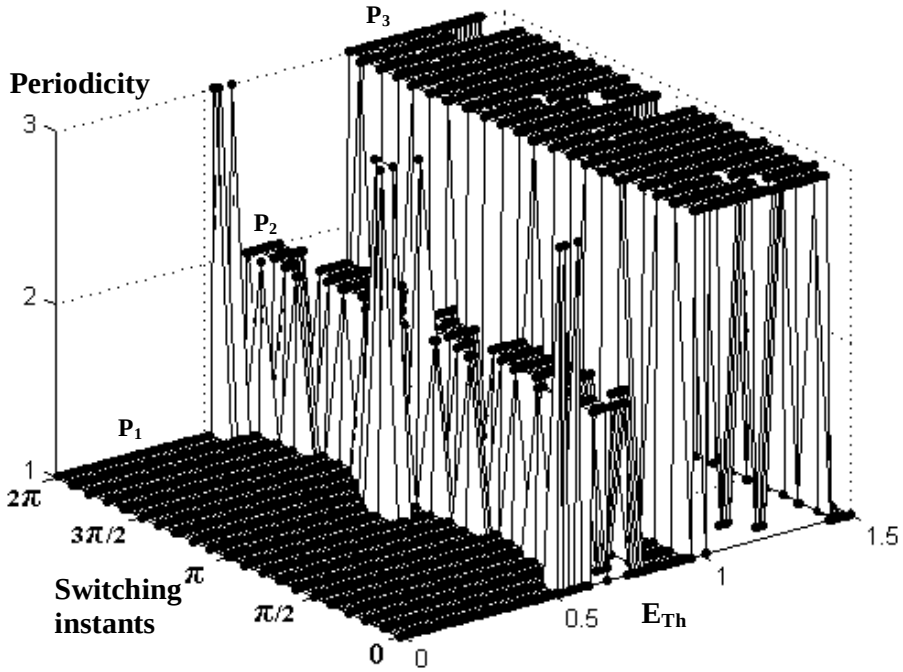

Fig.7.10b Temporal bifurcation diagram for Case D.1.2. (q = 7, R_m = 600, with arrester, C_{Th} = 0.047).
P_1 – fundamental solution, P_2 and P_3 – isolated subharmonic solutions.

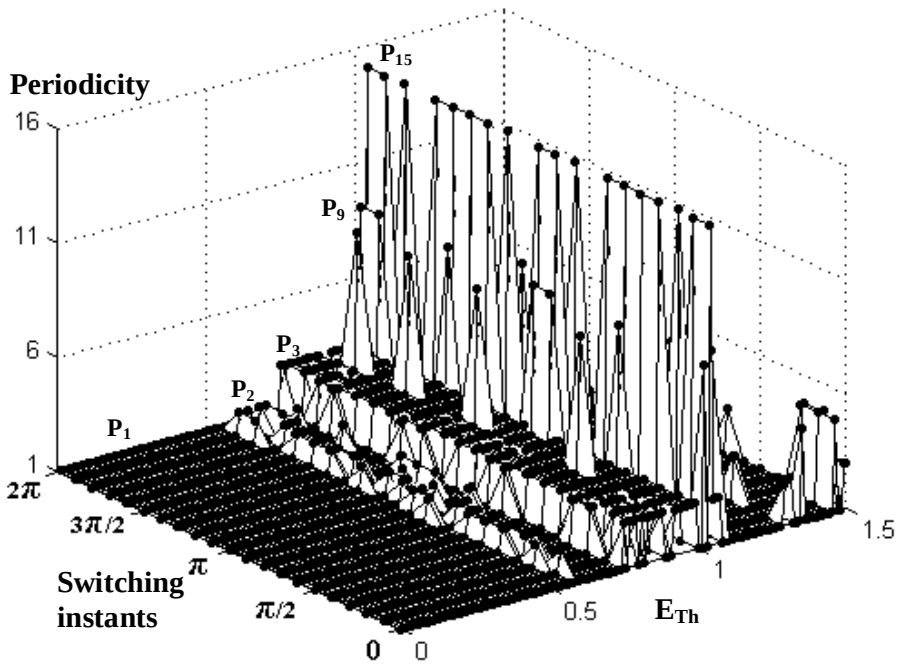

Fig.7.10c Temporal bifurcation diagram for Case D.1.3. (q = 11, R_m = 300, with arrester, C_{Th} = 0.047).
P_1 – fundamental solution, P_2, P_3, P_5, P_9 and P_{15} – isolated subharmonic solutions.

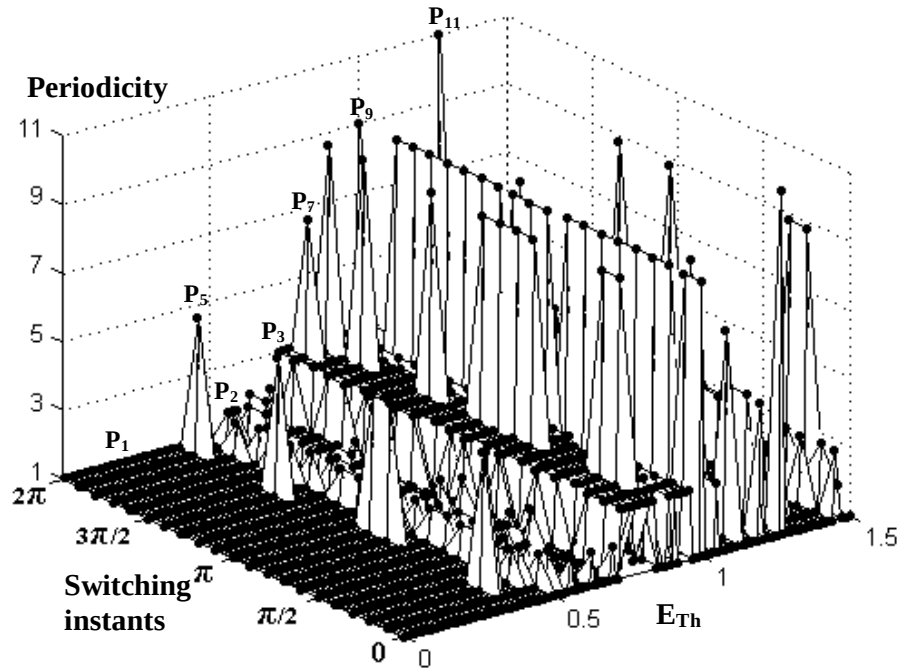

Fig.7.10d Temporal bifurcation diagram for Case D.1.4. (q = 11, R_m = 600, with arrester, C_{Th} = 0.047).
P_1 – fundamental solution, P_2, P_3, P_5, P_7, P_9 and P_{11} – isolated subharmonic solution.

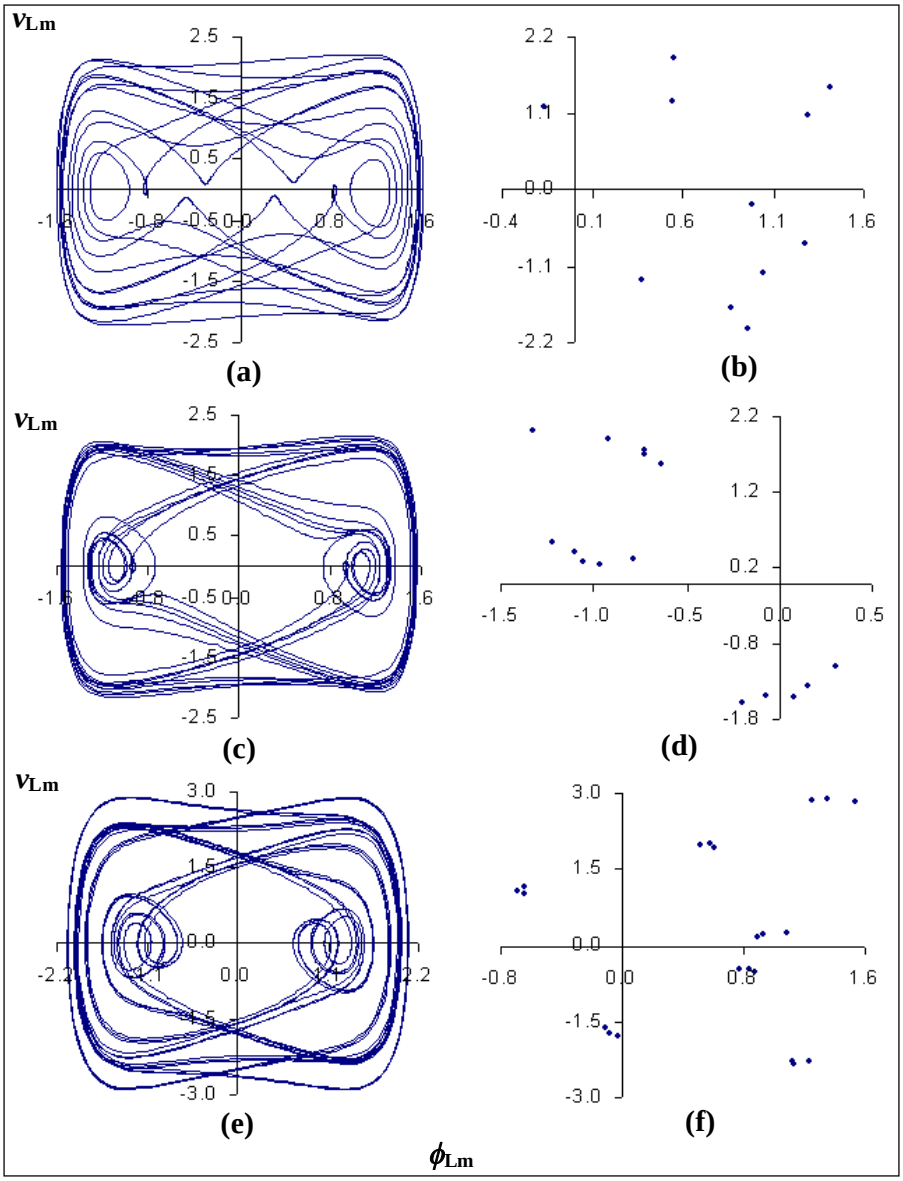

Fig.7.11 Phase plots and conventional Poincaré maps of subharmonic solutions.

(a) Phase plot of P_{11} oscillation, Fig.7.9b at E_{Th} = 1.190 p.u., t_{sw} = 0.6283 rad.

(b) Poincaré map of P_{11} oscillation, Fig.7.11a.

(c) Phase plot of P_{15} oscillation, Fig.7.10c at E_{Th} = 1.040 p.u., t_{sw} = 6.2831 rad.

(d) Poincaré map of P_{15} oscillation, Fig.7.11c.

(e) Phase plot of P_{21} oscillation, Fig.7.7a at E_{Th} =1.05 p.u., t_{sw} = 3.1415 rad.

(f) Poincaré map of P_{21} oscillation, Fig.7.11e.

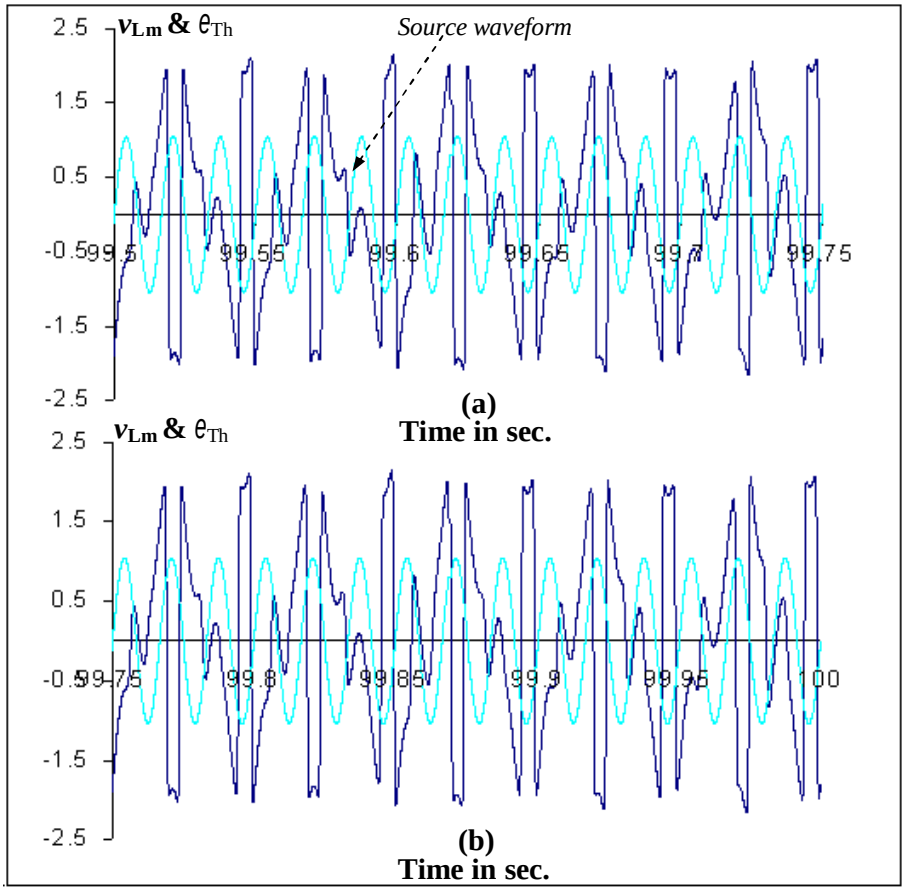

Fig.7.12 Time plot of the period 15 oscillation, Fig.7.11c, superimposed on the source waveform.

(a) From 5970 to 5985 cycles (99.5 to 99.75 seconds).

(b) From 5985 to 6000 cycles (99.75 to 100.0 seconds).

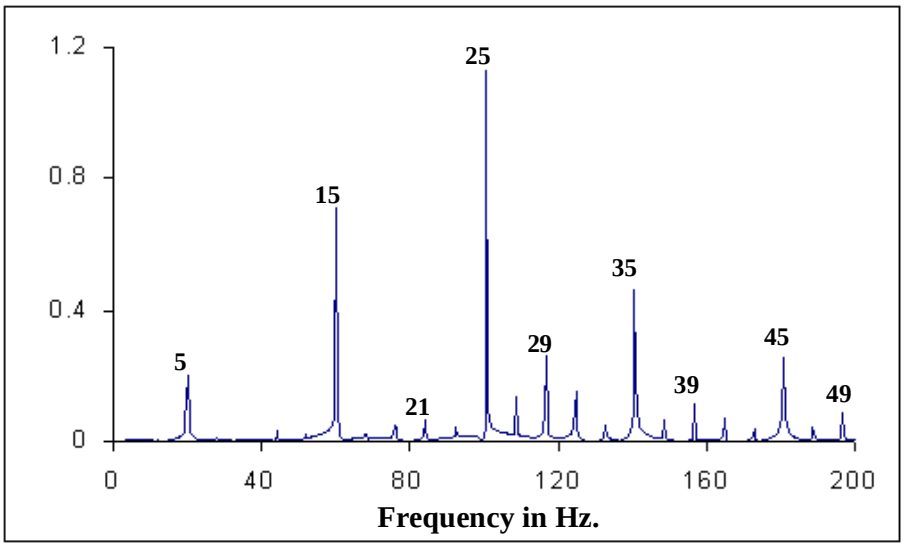

Fig.7.13 Fourier spectrum of period 15 oscillation, Fig.7.11c. Base frequency = 60/15 = 4.0 Hz. Number above peaks denote multiples of base frequency.

7.4 ANALYSIS OF ISOLATED SUBHARMONIC SOLUTIONS

The bifurcation diagrams of steady state solutions for various subharmonics have been generated for which the initial steady states obtained from temporal bifurcation diagrams. The bifurcation diagrams of steady state solutions depict the continuum of isolated subharmonic solutions for a range of bifurcation parameter (E_{Th}).

7.4.1 Effect of arrester on isolated subharmonic solutions

Figure 7.14 shows the continuum of period 2 solution for without arrester case (Case A.1.1), which forms a loop. Figures 7.15a to 7.15c depict the phase plots of period 2 oscillations at different points (in segments P_{2a}, P_{2b} and P_{2c} in Fig.7.13) on the loop. Interestingly, banded chaotic solutions are obtained in the flip segment of period 2 subharmonic solution path. Extensive analysis reveals the solution sequence in the flip segment as: period doubling cascade, banded chaotic solutions, unstable solutions, banded chaotic solutions and reverse bifurcations. Fig.7.16 shows the plot of Lyapunov exponents corresponding to flip segment F of Fig.7.14. The chaotic solutions occur on either side of flip segment F. Figures 7.17a to 7.17d show the phase plots and Poincaré maps of 4-band chaotic attractor on either side of segment F.

The inclusion of arrester (Case C.1.1) completely eliminates the period 2 oscillations, which can be observed from the temporal bifurcation diagram, Fig.7.6b. Figures 7.18 and 7.19 show the superimposed diagram of bifurcation diagram of steady state period 2 solutions for with and without arrester cases. Figure 7.18 clearly brings out the effectiveness of arrester in shrinking the region of subharmonic solutions (q = 11). The effectiveness of arrester in eliminating subharmonic flip segment (q = 7) is shown in Figure 7.19.

Figures 7.20 and 7.21 depict the bifurcation diagrams of period 3 solutions for Cases B.1.3 (without arrester) and D.1.3 (with arrester) respectively. The solution sequence in a subharmonic flip segment can be identified by hybrid bifurcation diagram. The hybrid bifurcation diagrams corresponding to flip segment F in figures are shown in Fig.7.22 and 7.23. It can be observed from these figures that though flip segment is reduced in the presence of arrester, banded chaotic solutions although interrupted are not eliminated. The plot of Lyapunov exponents shown in Fig.7.24 confirms the existence of chaotic solutions when arrester is present. The conventional Poincaré maps of 3-band chaotic attractor solutions are shown in Fig.7.25a and Fig.7.25b.

Figures 7.26 and 7.27 show the bifurcation diagram of period 5 solutions for Cases A.1.4 (without arrester) and C.1.4 (with arrester) respectively. They confirm the contraction of subharmonic solution when arrester is included.

Figures 7.28 and 7.29 show the bifurcation diagrams of period 9 and period 11 solutions (Case C.1.4, with arrester) respectively. Banded chaotic solutions are obtained in both the cases. Figures 7.30a to 7.30f depict the phase plots and conventional Poincaré maps of period 9, period 11 and banded chaotic solutions.

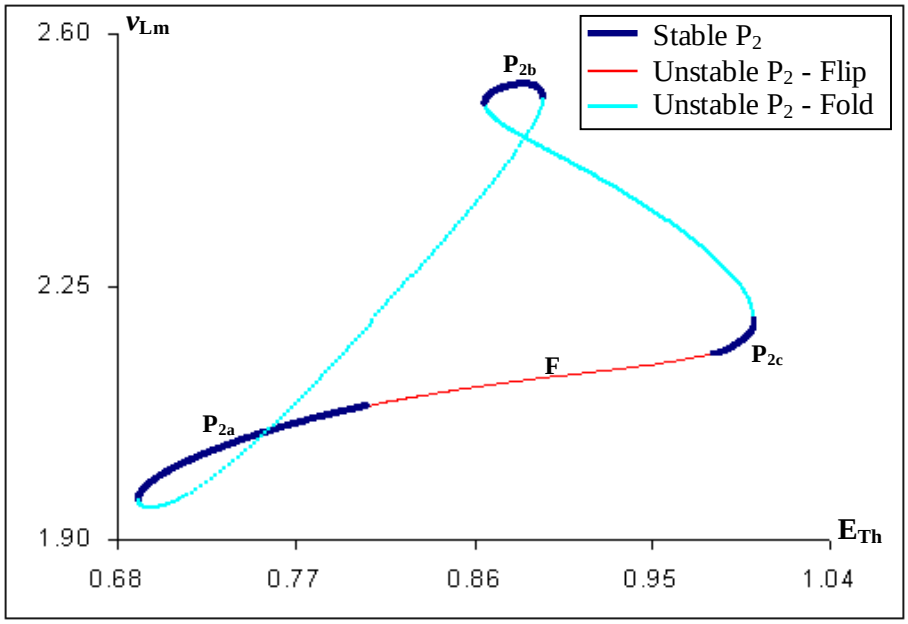

Fig.7.14 Bifurcation diagram of steady state P_2 solution: q = 7, R_m = 300, C_{Th} = 0.0616, without arrester (Case A.1.1). Initial steady state is obtained from temporal bifurcation diagram, Fig.7.6a.

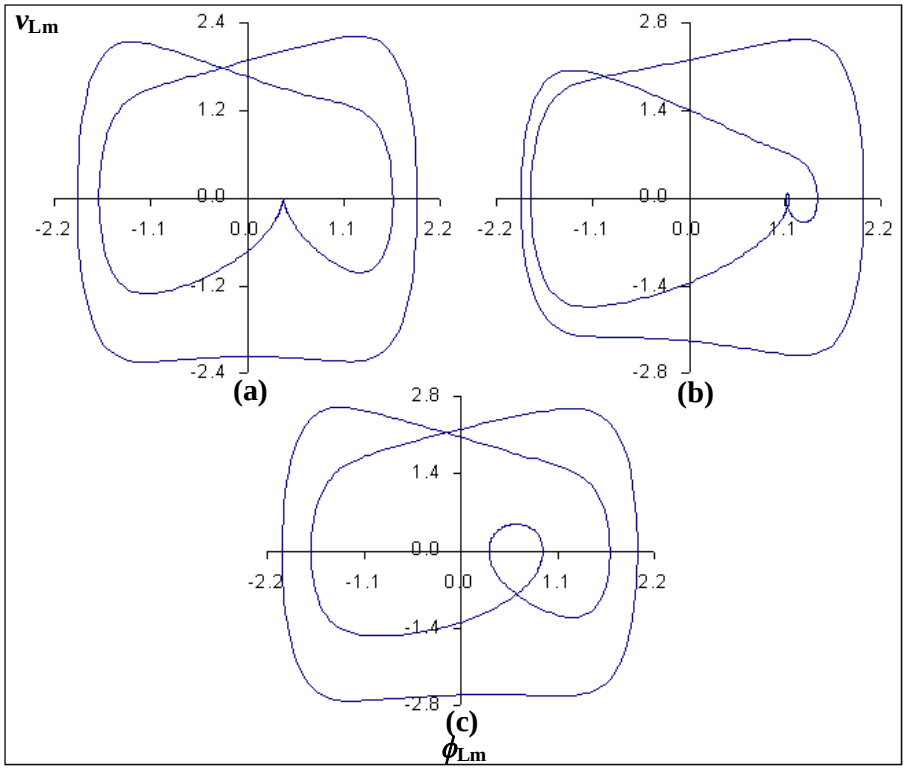

Fig.7.15 Phase plots of P_2 oscillations at different points on the solution loop, Fig.7.14.

(a) At E_{Th} = 0.775818 p.u. (In P_{2a}). (b) At E_{Th} = 0.88504 p.u. (In P_{2b}).

(c) At E_{Th} = 0.99594 p.u. (In P_{2c}).

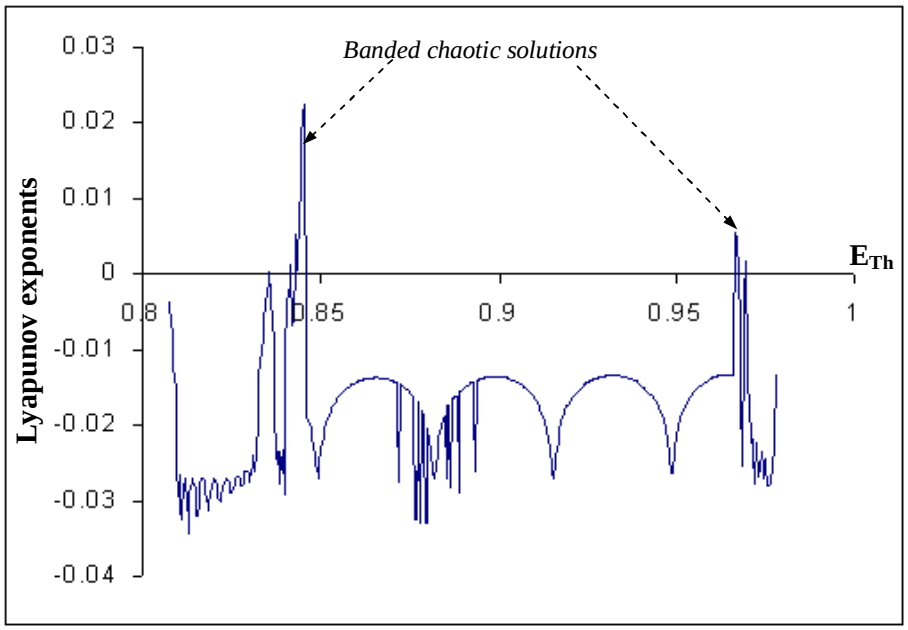

Fig.7.16 Plot of Lyapunov exponents corresponding to the flip segment F in Fig.7.14.

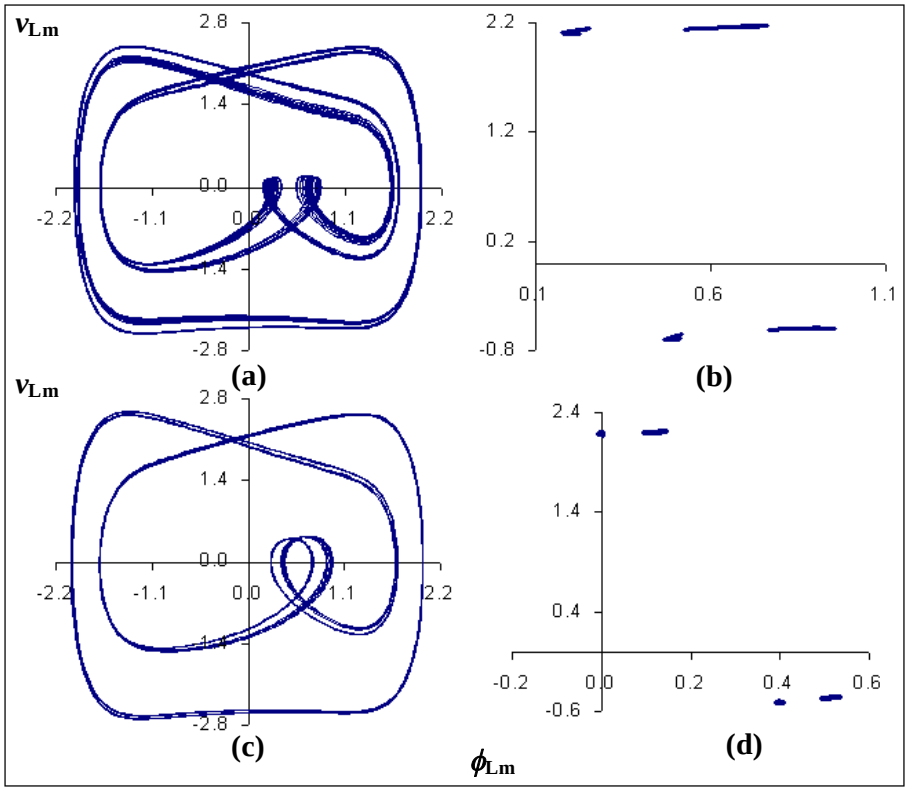

Fig.7.17 Phase plots and conventional Poincaré maps of 4-band attractor.
(a), (c) Phase plots at E_{Th} = 0.845176 and E_{Th} = 0.966646 p.u., Fig.7.14.
(b), (d) Poincaré maps of Figures 7.17a and 7.17c.

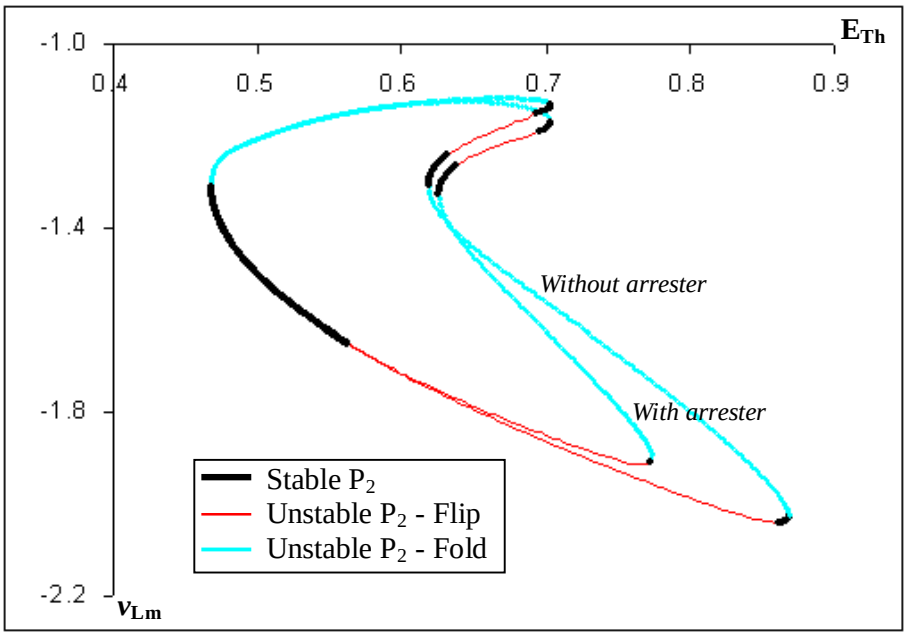

Fig.7.18 Bifurcation diagrams of steady state period 2 solutions: q = 11, R_m = 600, C_{Th} = 0.047, with and without arrester (Cases D.1.4 and B.1.4). Initial steady states are obtained from temporal bifurcation diagrams, Figures 7.9a and 7.9b.

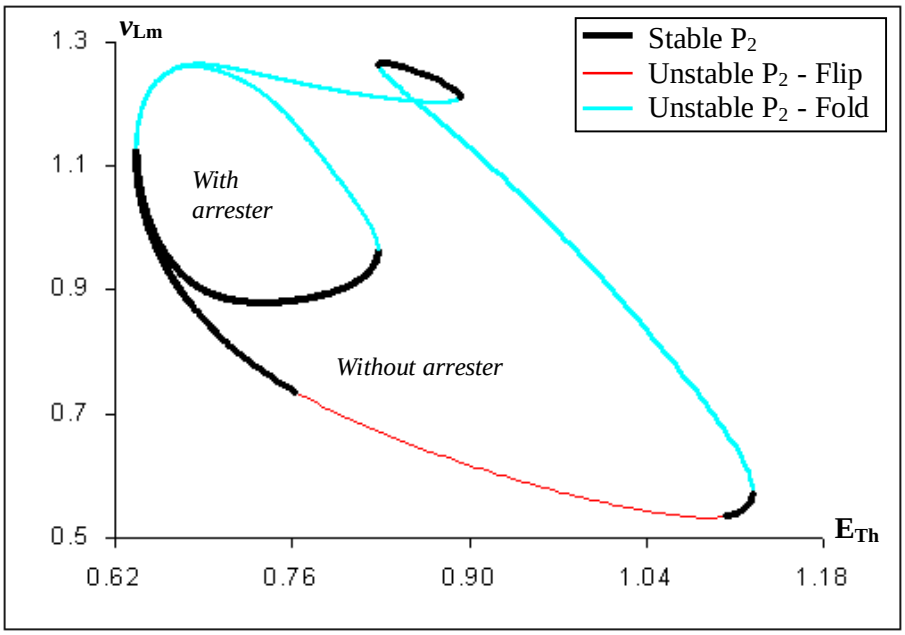

Fig.7.19 Bifurcation diagrams of steady state period 2 solutions: q = 7, R_m = 600, C_{Th} = 0.0616, with and without arrester (Cases C.1.2 and A.1.2). Initial steady states are obtained from temporal bifurcation diagrams, Figures 7.7a and 7.7b.

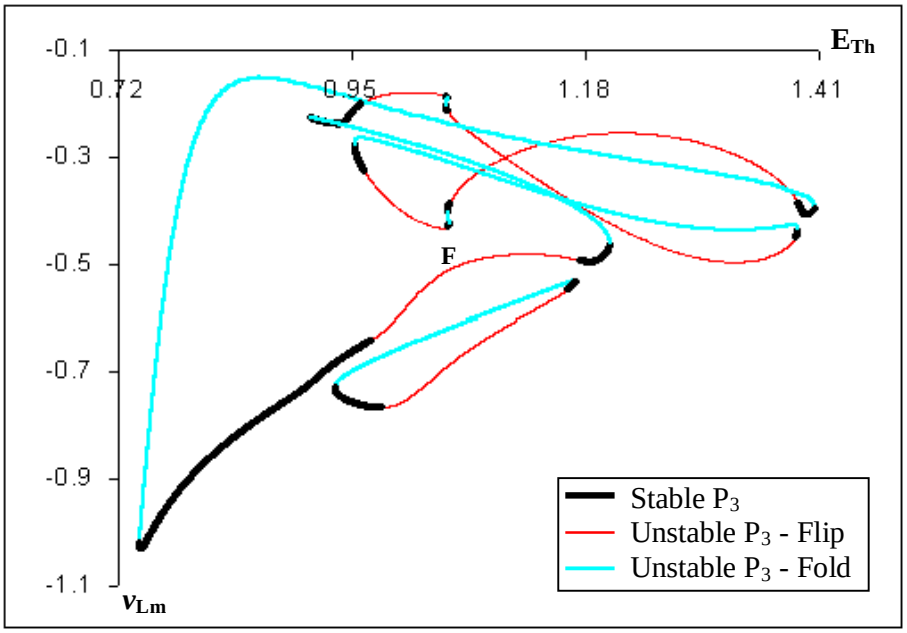

Fig.7.20 Bifurcation diagram of steady state period 3 solution: q = 11, R_m = 300, without arrester, C_{Th} = 0.047 (Case B.1.3). Initial steady state is obtained from temporal bifurcation diagram, Fig.5.7c (Chapter 5).

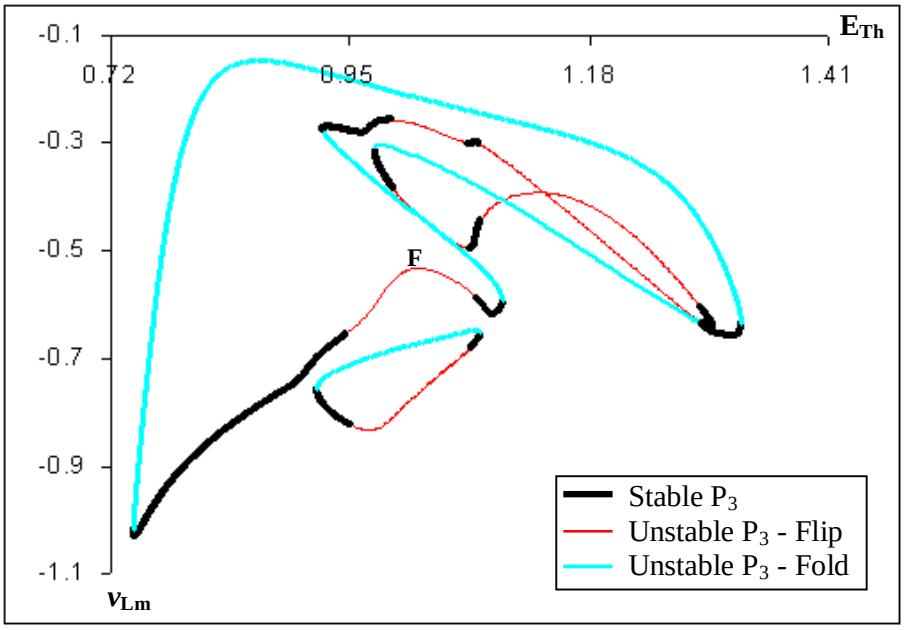

Fig.7.21 Bifurcation diagram of steady state period 3 solution: q = 11, R_m = 300, with arrester, C_{Th} = 0.047 (Case D.1.3). Initial steady state is obtained from temporal bifurcation diagram, Fig.7.10c.

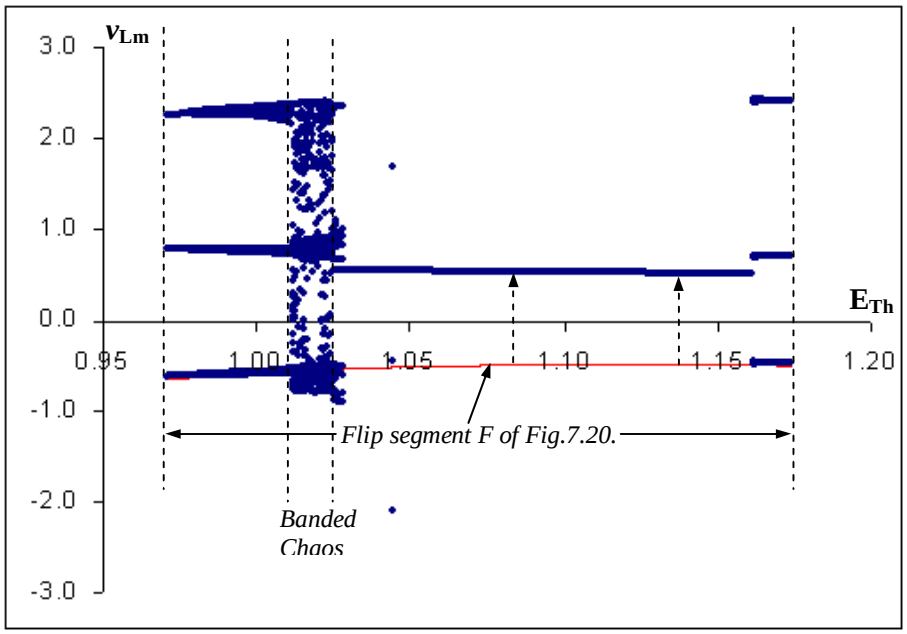

Fig.7.22 Hybrid bifurcation diagram corresponding to flip segment F in Fig.7.20. (q = 11, R_m = 300, without arrester, C_{Th} = 0.047).

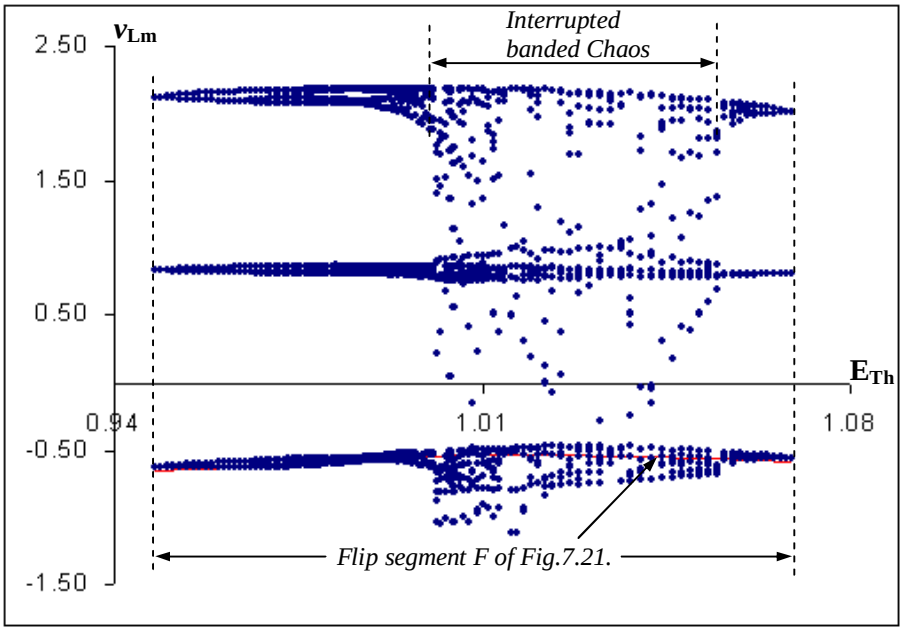

Fig.7.23 Hybrid bifurcation diagram corresponding to flip segment F in Fig.7.21. (q = 11, R_m = 300, with arrester, C_{Th} = 0.047).

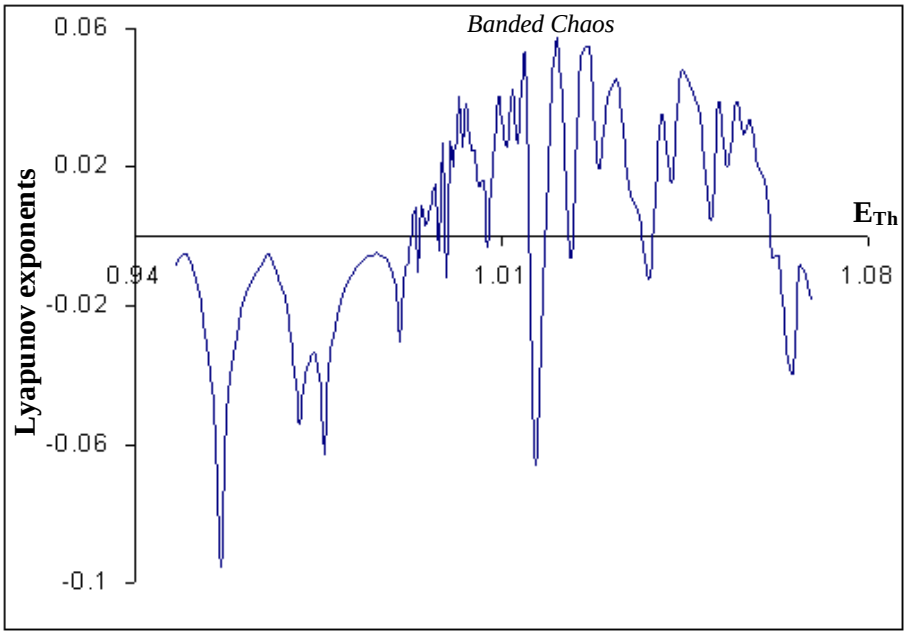

Fig.7.24 Plot of Lyapunov exponents corresponding to flip segment F in Fig.7.21 (q = 11, R_m = 300, without arrester, C_{Th} = 0.047).

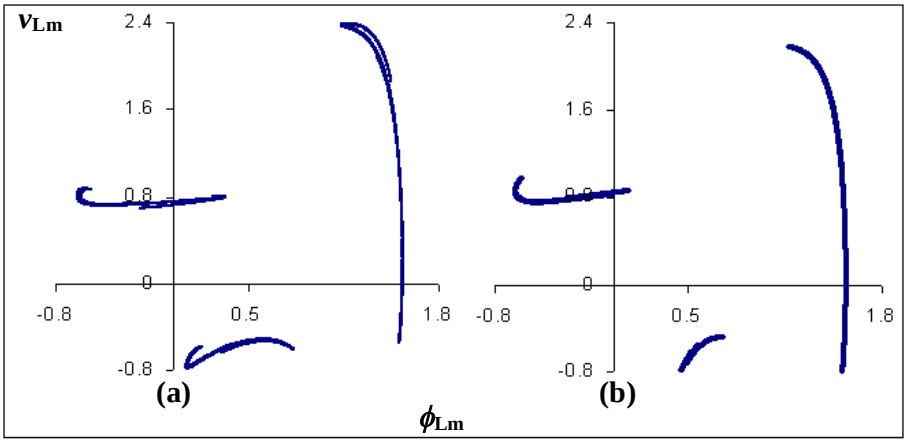

Fig.7.25 Conventional Poincaré maps of 3-band chaotic attractor:

(a) At E_{Th} = 1.014223 p.u, without arrester case, Fig.7.22.

(b) At E_{Th} = 1.014148 p.u. with arrester case, Fig.7.23.

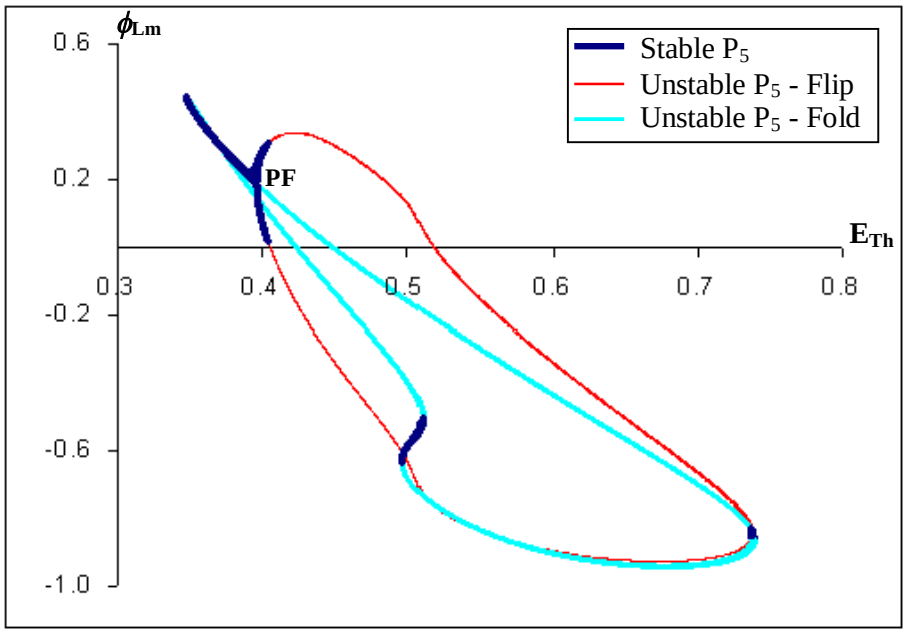

Fig.7.26 Bifurcation diagram of steady state P_5 solution: q = 11, R_m = 600, without arrester, C_{Th} = 0.0616 (Case A.1.4). Initial steady state is obtained from temporal bifurcation diagram, Fig.7.9a. PF – supercritical pitchfork bifurcation point.

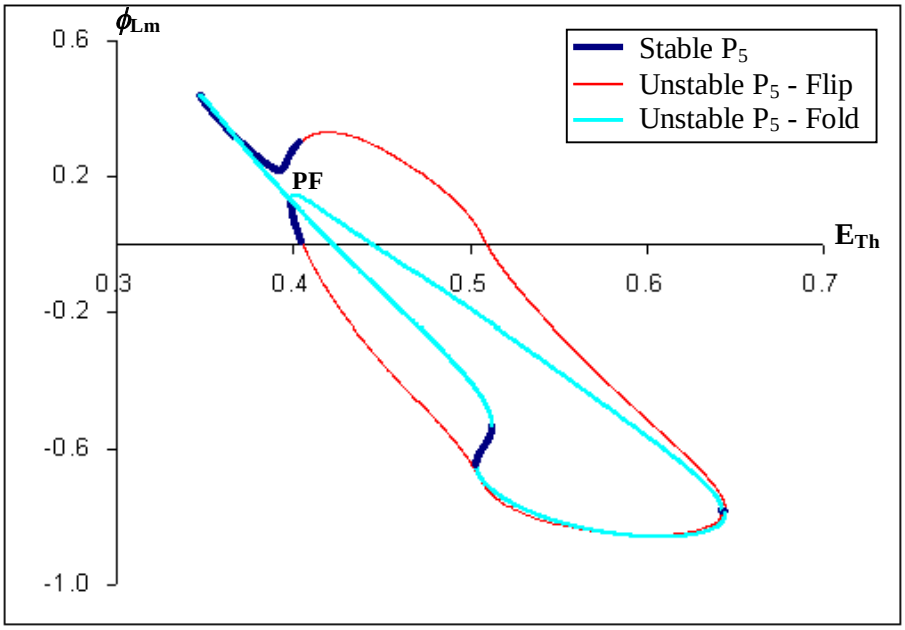

Fig.7.27 Bifurcation diagram of steady state P_5 solution: q = 11, R_m = 600, with arrester, C_{Th} = 0.0616 (Case C.1.4). Initial steady state is obtained from temporal bifurcation diagram, Fig.7.9b. PF – supercritical pitchfork bifurcation point.

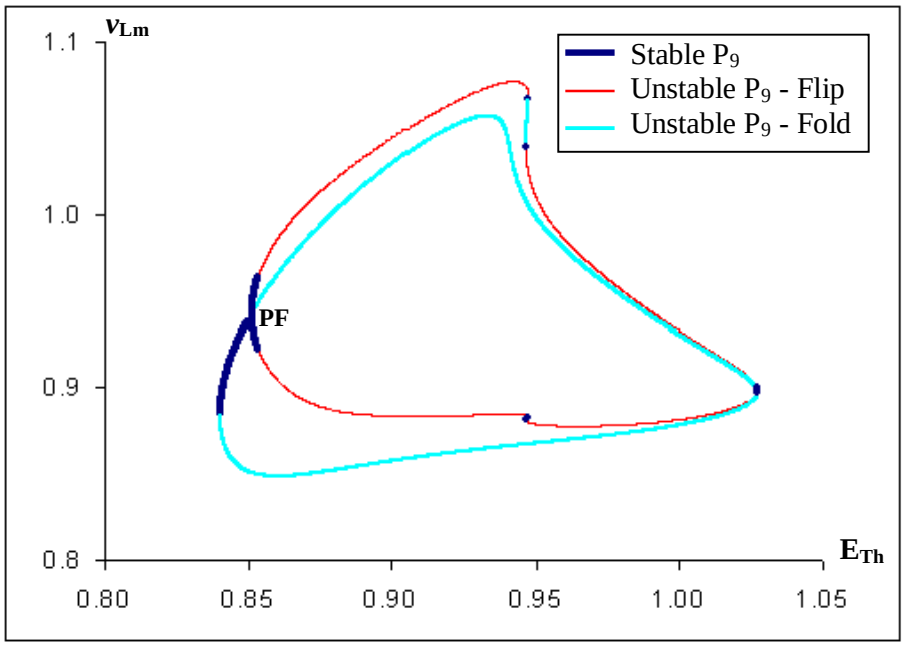

Fig.7.28 Bifurcation diagram of steady state P_9 solution: q = 11, R_m = 600, with arrester, C_{Th} = 0.0616 (Case C.1.4). Initial steady state is obtained from temporal bifurcation diagram, Fig.7.9b. PF – supercritical pitchfork bifurcation point.

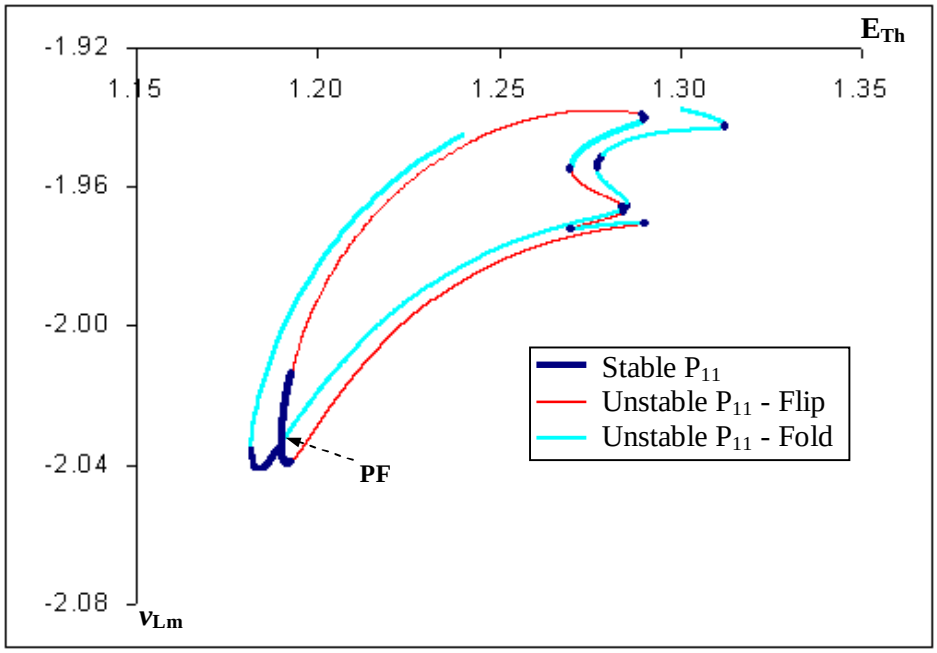

Fig.7.29 Bifurcation diagram of steady state P_{11} solution: q = 11, R_m = 600, with arrester, C_{Th} = 0.0616 (Case C.1.4). Initial steady state is obtained from temporal bifurcation diagram, Fig.7.9b. PF – supercritical pitchfork bifurcation.

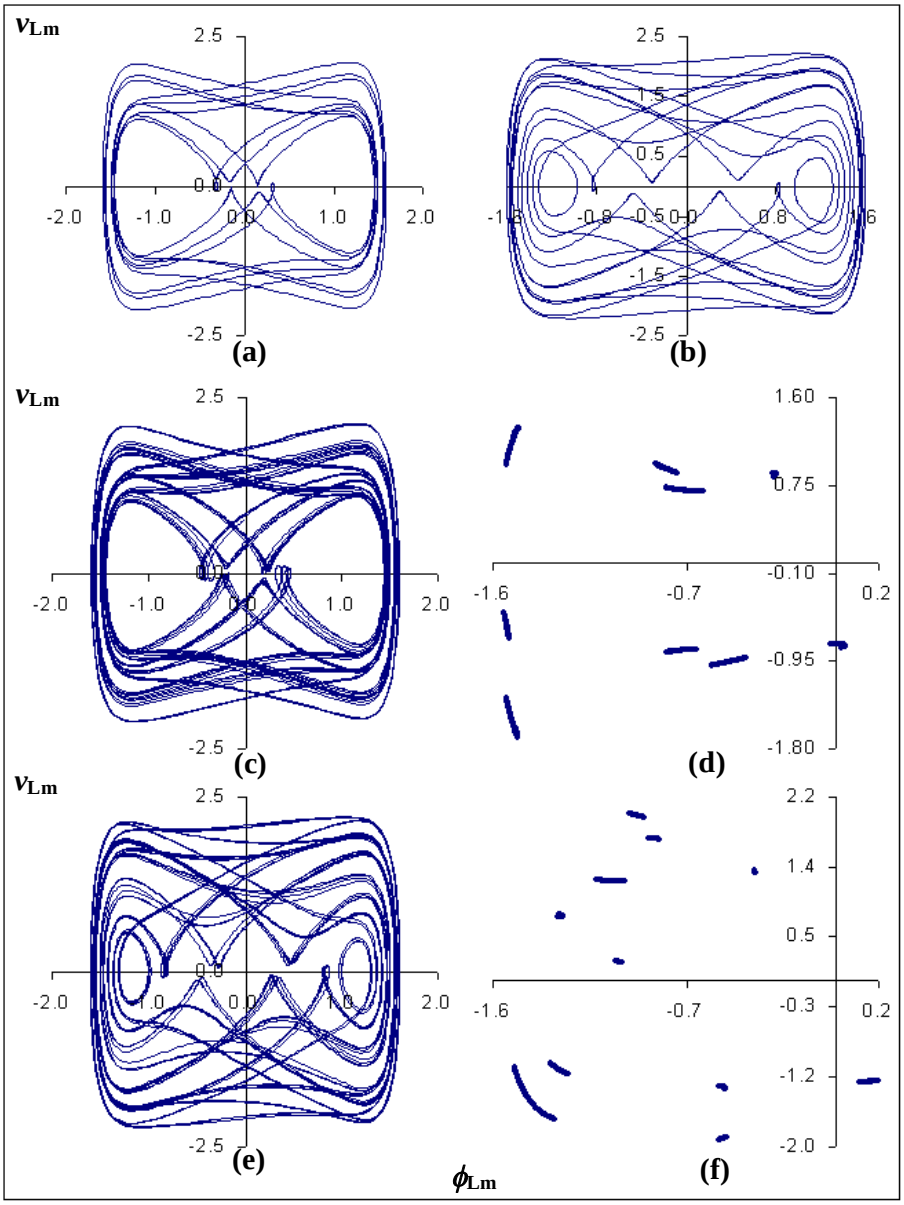

Fig.7.30 Phase plots and Conventional Poincaré maps of P_9, P_{11} and banded chaotic oscillations.

(a) Phase plot of P_9 oscillation at E_{Th} = 0.842031 p.u., Fig.7.28.
(b) Phase plot of P_{11} oscillation at E_{Th} = 1.182151 p.u., Fig.7.29.
(c) Phase plot of 9-band chaos at E_{Th} = 0.855186 p.u., Fig.7.28.
(d) Conventional Poincaré map of 9-band chaos, Fig.7.30c.
(e) Phase plot of 11-band chaos at E_{Th} = 1.195779 p.u., Fig.7.29.
(f) Conventional Poincaré map of 11-band chaos, Fig.7.30e.

7.4.2 Effect of core loss on isolated subharmonic solutions

From Tables 7.5 to 7.8 it can be concluded that in general lower core loss (higher the core loss resistance value) results in higher order subharmonic solutions. For example, period 21 solution is obtained for lower core loss case (Case A.1.2) and is absent for higher core loss (Case A.1.1). Figure 7.31 shows the continuum of period 21 solution. The conventional Poincaré map of 21-band attractor, encountered in the flip segment F of Fig.7.31 at E_{Th} = 1.050337 p.u., is shown in Fig.7.32.

Further, lower core loss increases the number of solutions and the number of bifurcations as can be seen from Fig.7.34. Table 7.9 compares the lower and higher core loss cases.

Table 7.9 Comparison of results obtained for lower and higher core loss cases.

Core loss	Case number / description	Figure number	Observation
R_m = 300 (high)	Case B.1.1 q = 7, without arrester, C_{Th} = 0.0616	Fig.7.33 (continuum of P_3)	No flip and pitchfork bifurcation
R_m = 600 (low)	Case B.1.2 q = 7, without arrester, C_{Th} = 0.047	Fig.7.34 (continuum of P_3) Fig.7.35 (plot of Lyapunov exponents) Fig.7.36 (phase plots)	More number of solutions and bifurcations (flip, pitchfork). Occurrence of banded chaos.
R_m = 300 (high)	Case B.1.3 q = 11, without arrester, C_{Th} = 0.047	Fig.7.37 (continuum of P_9)	Less number of solutions and bifurcations (flip, fold). Occurrence of banded chaos.
R_m = 600 (low)	Case B.1.4 q = 11, without arrester, C_{Th} = 0.047	Fig.7.38 (continuum of P_9)	More number of solutions and bifurcations (flip, fold). Occurrence of banded chaos.

The plot of Lyapunov exponents corresponding to flip segment F in Fig.7.34 is shown in Fig.7.36. It confirms the existence of chaotic solution. Fig.7.36a to Fig.7.36d show the phase plots of symmetric P_3, unsymmetric P_3, P_6 and 3-band chaotic solutions.

7.4.3 Effect of core saturation on isolated subharmonic solutions

Higher core saturation index makes the occurrence of subharmonic solutions and bifurcations at a lower value of bifurcation parameter. Also, the number of bifurcations in the continuum of solution is increased in this case. The representative cases, figure numbers and observations are summarised in Table 7.10.

Table 7.10 Comparison of results obtained for lower and higher core saturation indices.

Saturation index	Case number / description	Figure number	Observation
q = 7	Case B.1.2 R_m = 600, without arrester, C_{Th} = 0.047	Fig.7.39 (continuum of P_9)	Less number of bifurcations (flip, fold). Solutions start at higher value of $E_{Th.}$
q = 11	Case B.1.4 R_m = 600, without arrester, C_{Th} = 0.047	Fig.7.38 (continuum of P_9)	More number of bifurcations (flip, fold). Solutions start at lower value of $E_{Th.}$
q = 7 and q =11	Case B.1.3 R_m = 300, without arrester, C_{Th} = 0.047	Fig.7.40 (continuum of P_2 solutions superimposed)	Solutions start at lower value of E_{Th} (q = 11). Increased unstable segments (q = 11).
q = 7	Case B.1.2 R_m = 600, without arrester, C_{Th} = 0.047	Fig.7.41 (continuum of P_5)	Solutions start at higher value of $E_{Th.}$
q = 11	Case B.1.4 R_m = 600, without arrester, C_{Th} = 0.047	Fig.7.42 (continuum of P_5)	Solutions start at lower value of E_{Th}

7.4.4 Effect of source capacitance on isolated subharmonic solutions

Higher source capacitance widens the range and multiplicity of subharmonic solutions. The effect of source capacitance is predominant in lower core saturation case. Table 7.11 summarises the representative cases, figure numbers and observations.

Table 7.11 Summary of results obtained for lower and higher source capacitances.

Source capacitance (C_{Th})	Case number / description	Figure number	Observation
0.0616	Case B.1.2 q = 7, R_m = 600, without arrester	Fig.7.44 (continuum of P_7) Fig.7.46 (7-band chaos)	Range of subharmonics is more. Number of solutions and bifurcations are more.
0.047	Case A.1.2 q = 7, R_m = 600, without arrester	Fig.7.43 (continuum of P_7) Fig.7.45 (7-band chaos)	Range of subharmonics is less. Number of solutions and bifurcations are less.
0.0616	Case B.1.4 q = 11, R_m = 600, without arrester	Fig.7.47 (continuum of P_3)	Range of subharmonics is more.
0.047	Case A.1.4 q = 11, R_m = 600, without arrester	Fig.7.48 (continuum of P_3)	Range of subharmonics is less.

The 7-band chaotic solutions are obtained in the continuum of period 7 solution for both lower and higher source capacitances. The phase plots of 7-band attractor are shown in Figures 7.45 and 7.46.

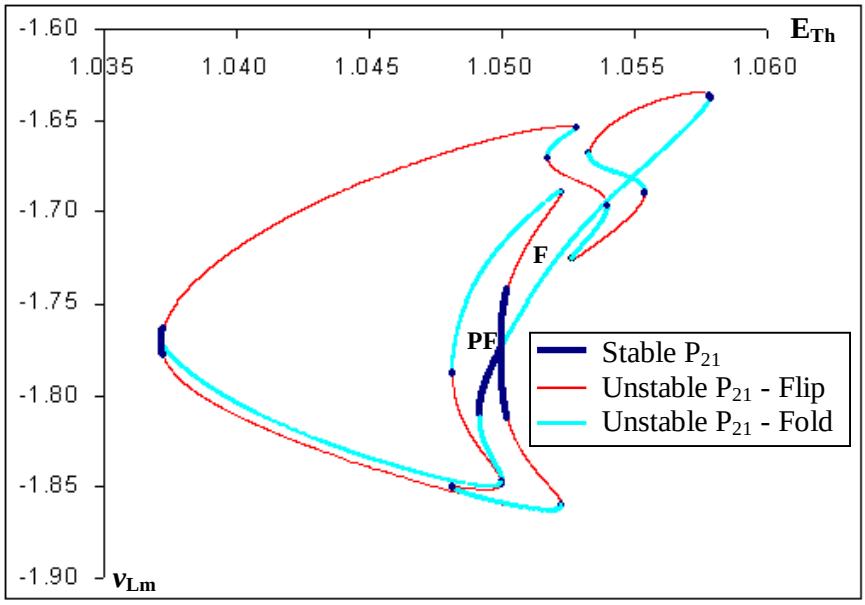

Fig.7.31 Bifurcation diagram of steady state P_{21} solution: q = 7, R_m = 600, without arrester, C_{Th} = 0.0616 (Case A.1.2). Initial steady state is obtained from temporal bifurcation diagram, Fig.7.7a. PF – supercritical pitchfork bifurcation point.

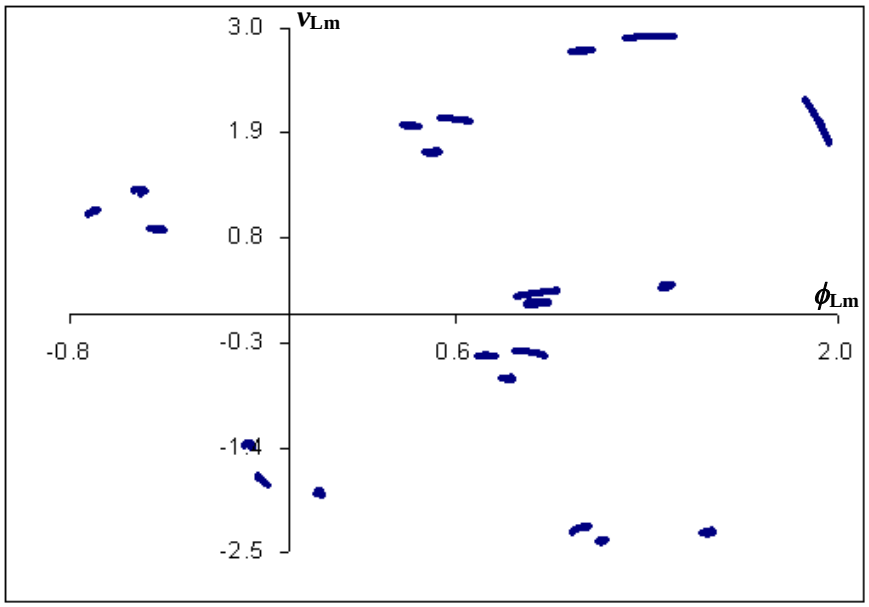

Fig.7.32 Conventional Poincaré map of 21-band attractor at E_{Th} = 1.050337 p.u. in flip segment F of Fig.7.31.

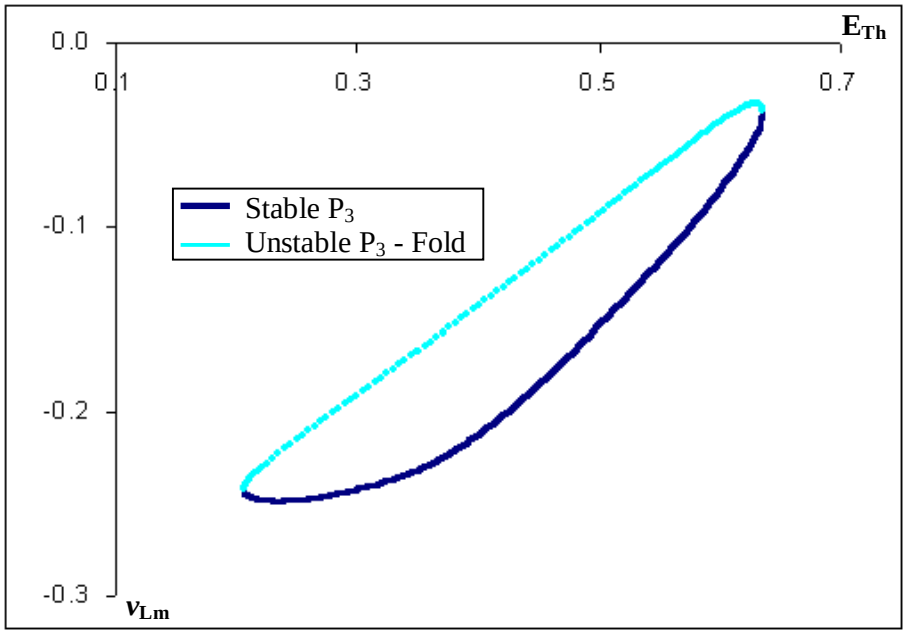

Fig.7.33 Bifurcation diagram of steady state P_3 solution: q = 7, R_m = 300, without arrester, C_{Th} = 0.047 (Case B.1.1). Initial steady state is obtained from temporal bifurcation diagram, Fig.5.7a (Chapter 5).

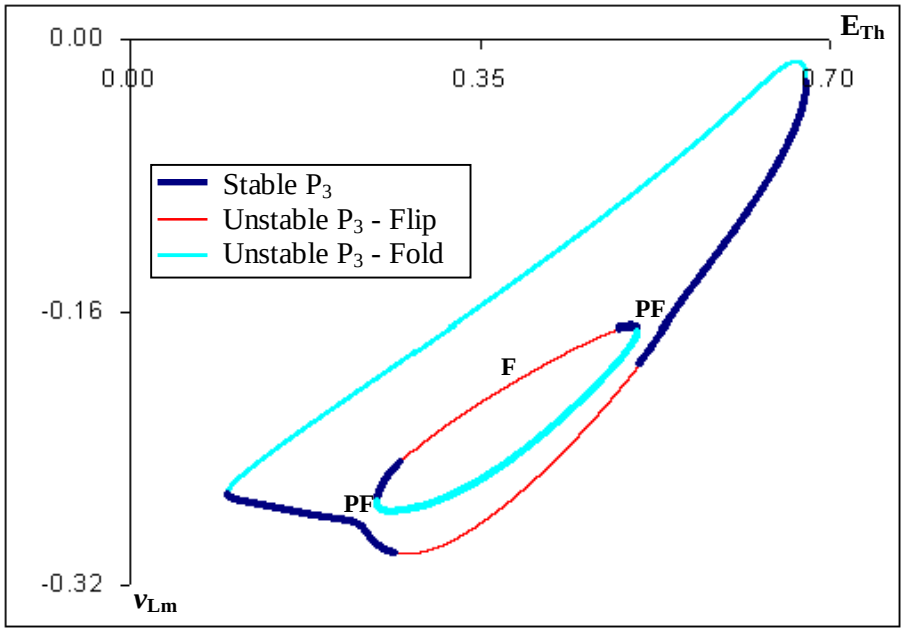

Fig.7.34 Bifurcation diagram of steady state P_3 solution: q = 7, R_m = 600, without arrester, C_{Th} = 0.047 (Case B.1.2). Initial steady state is obtained from temporal bifurcation diagram, Fig.5.7b (Chapter 5). PF – supercritical pitchfork bifurcation point.

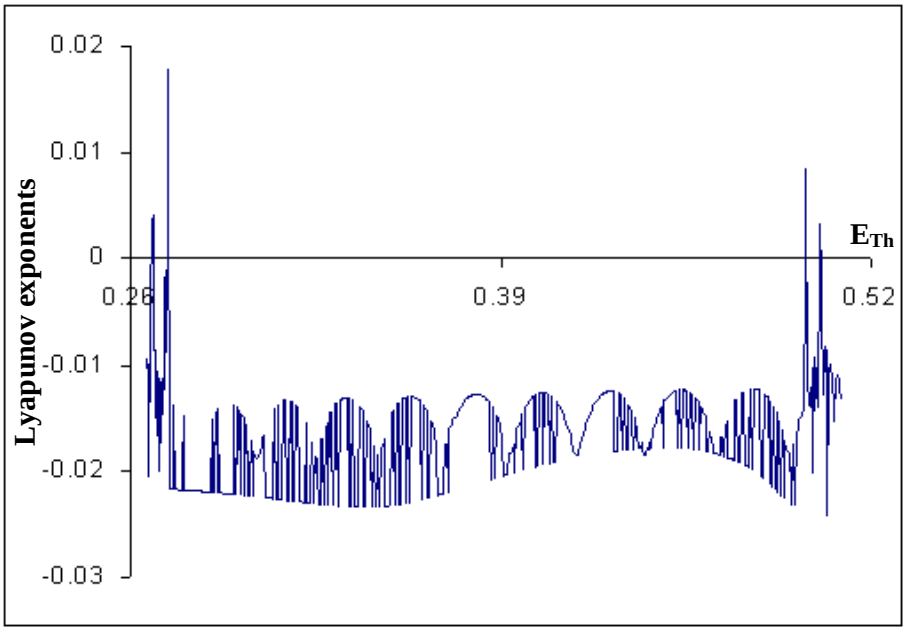

Fig.7.35 Plot of Lyapunov exponents corresponding to the flip segment F in Fig.7.34.

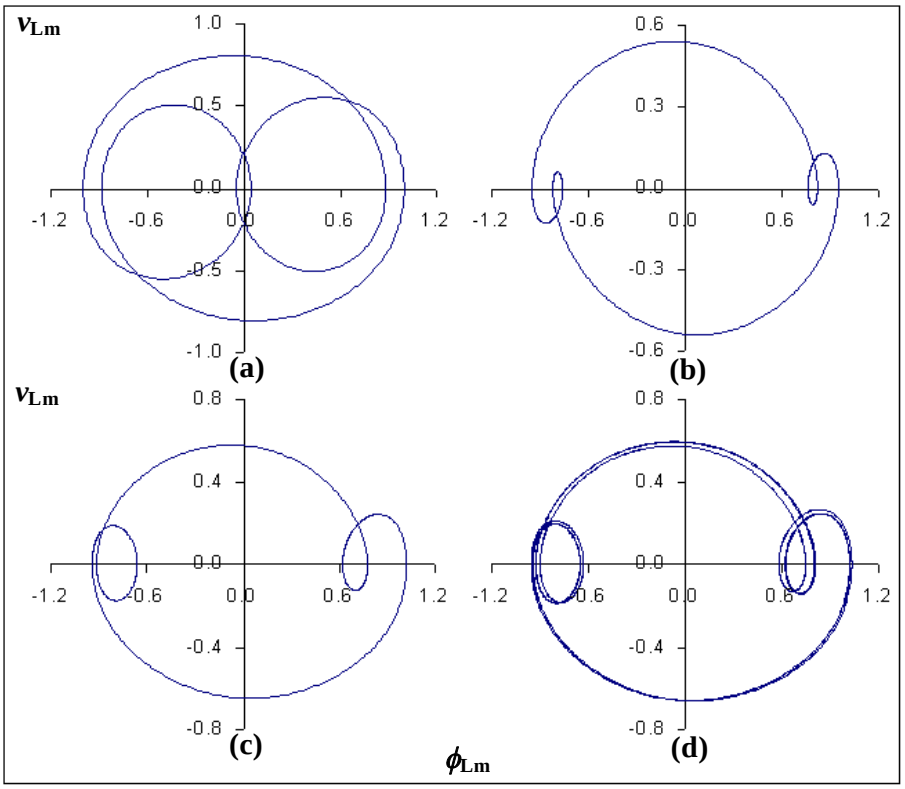

Fig.7.36 Phase plot of P_3, P_6 and chaotic solutions

(a) Symmetric P_3 solution at E_{Th} = 0.545 p.u., Fig.7.33.
(b) Symmetric P_3 solution at E_{Th} = 0.59656 p.u., Fig.7.34.
(c) Unsymmetric P_3 solution at E_{Th} = 0.264039 p.u., Fig.7.34.
(d) 3-band chaotic solution at E_{Th} = 0.273179 p.u., Fig.7.34.

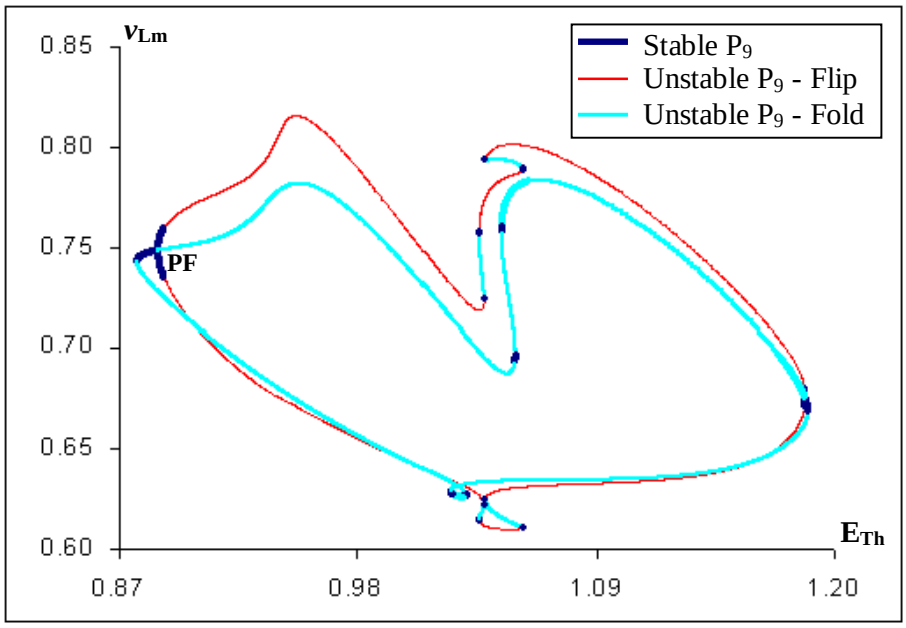

Fig.7.37 Bifurcation diagram of steady state P_9 solution: q = 11, R_m = 300, without arrester, C_{Th} = 0.047 (Case B.1.3). Initial steady state is obtained from temporal bifurcation diagram, Fig.5.7c (Chapter 5). PF – supercritical pitchfork bifurcation point.

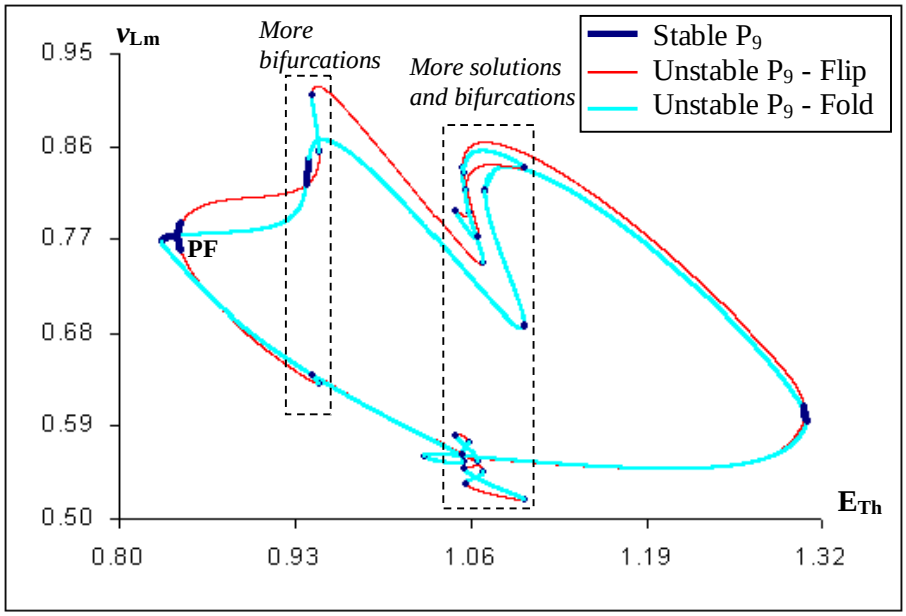

Fig.7.38 Bifurcation diagram of steady state P_9 solution: q = 11, R_m = 600, without arrester, C_{Th} = 0.047 (Case B.1.4). Initial steady state is obtained from temporal bifurcation diagram, Fig.5.7d (Chapter 5). PF – supercritical pitchfork bifurcation point.

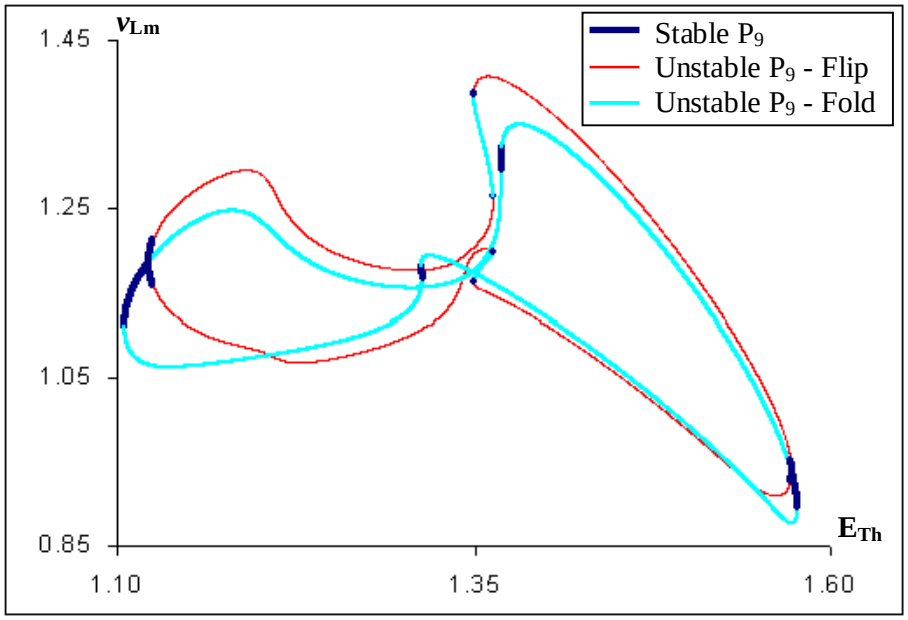

Fig.7.39 Bifurcation diagram of steady state P_9 solution: q = 7, R_m = 600, without arrester, C_{Th} = 0.047 (Case B.1.2). Initial steady state is obtained from temporal bifurcation diagram, Fig.5.7b (Chapter 5).

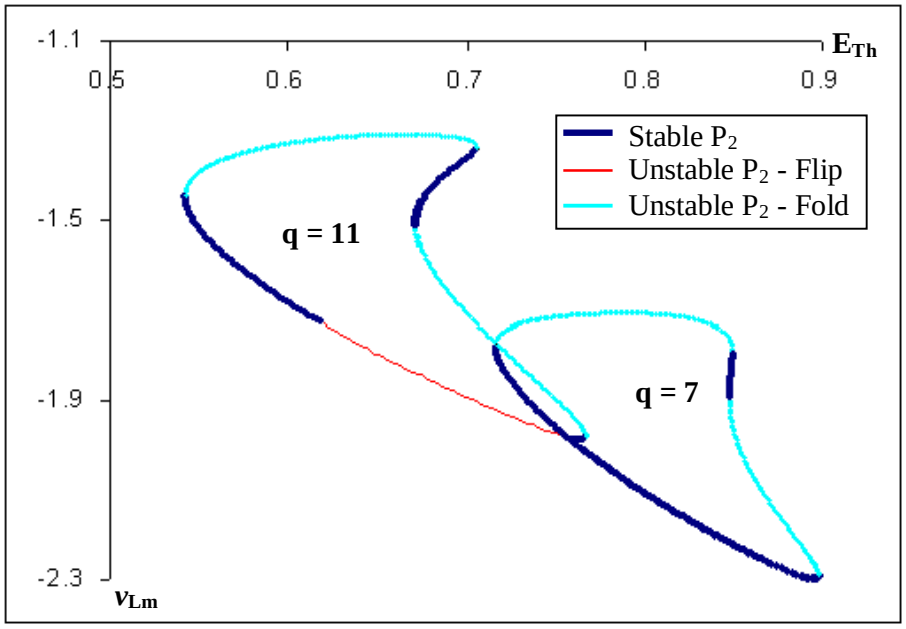

Fig.7.40 Superimposed diagram of steady state period 2 solutions: q = 7 and 11, R_m = 300, without arrester, C_{Th} = 0.047 (Cases B.1.1 and B.1.3). Initial steady states are obtained from temporal bifurcation diagrams, Fig.5.7a and Fig.5.7c (Chapter 5).

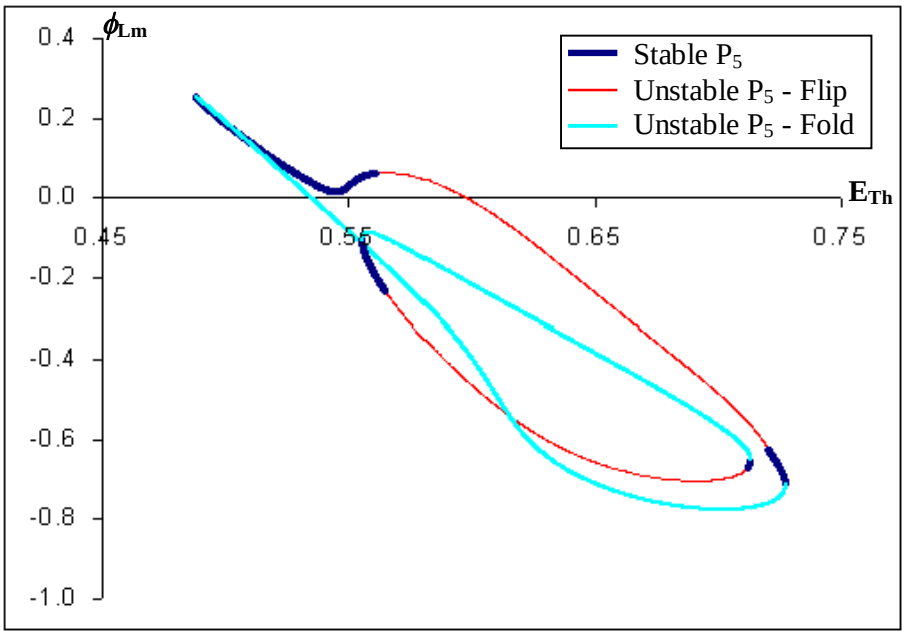

Fig.7.41 Bifurcation diagram of steady state P_5 solution: q = 7, R_m = 300, without arrester, C_{Th} = 0.047 (Case B.1.2). Initial steady state is obtained from temporal bifurcation diagram, Fig.5.7b (Chapter 5).

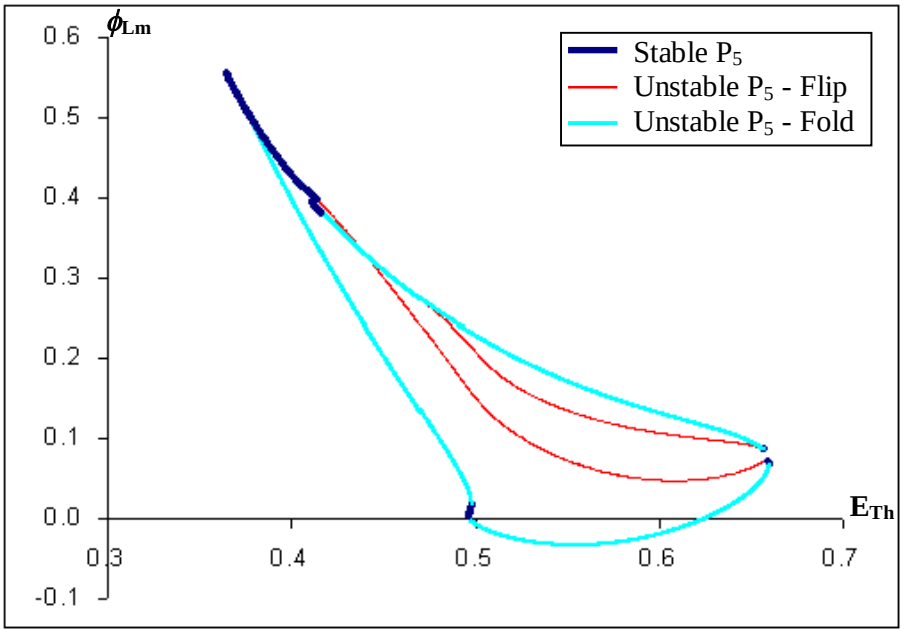

Fig.7.42 Bifurcation diagram of steady state P_5 solution: q = 11, R_m = 600, without arrester, C_{Th} = 0.047 (Case B.1.4). Initial steady state is obtained from temporal bifurcation diagram, Fig.5.7d (Chapter 5).

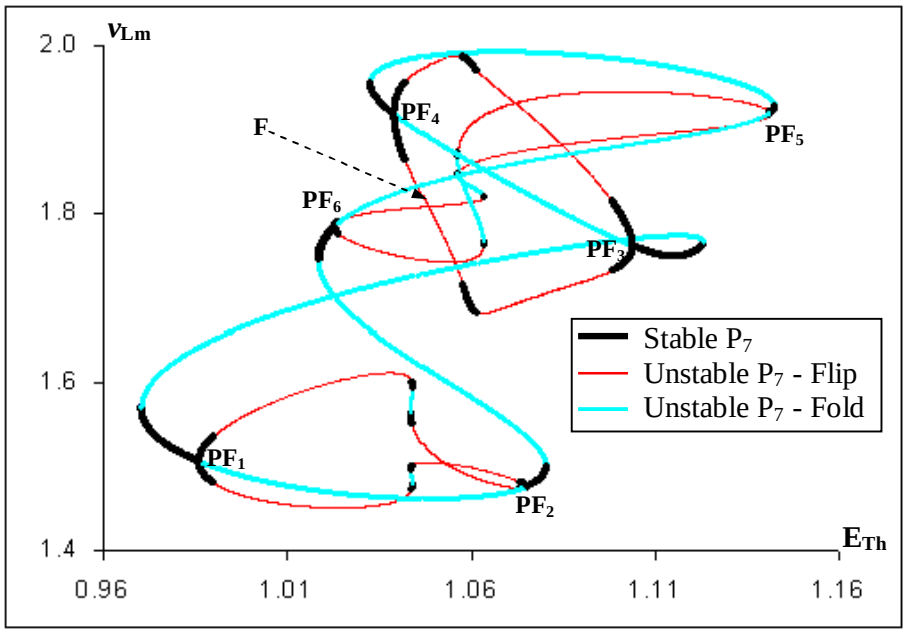

Fig.7.43 Bifurcation diagram of steady state P_7 solution: q = 7, R_m = 600, without arrester, C_{Th} = 0.0616 (Case A.1.2). Initial steady state is obtained from temporal bifurcation diagram, Fig.7.7a. PF – supercritical pitchfork bifurcation point.

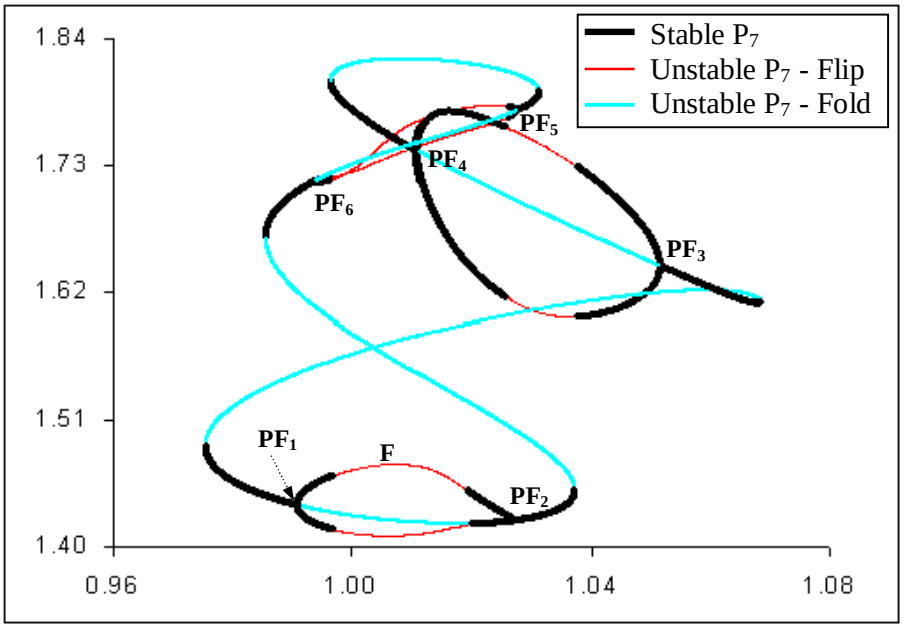

Fig.7.44 Bifurcation diagram of steady state P_7 solution: q = 7, R_m = 600, without arrester, C_{Th} = 0.047 (Case B.1.2). Initial steady state is obtained from temporal bifurcation diagram, Fig.5.7b (Chapter 5). PF – supercritical pitchfork bifurcation point.

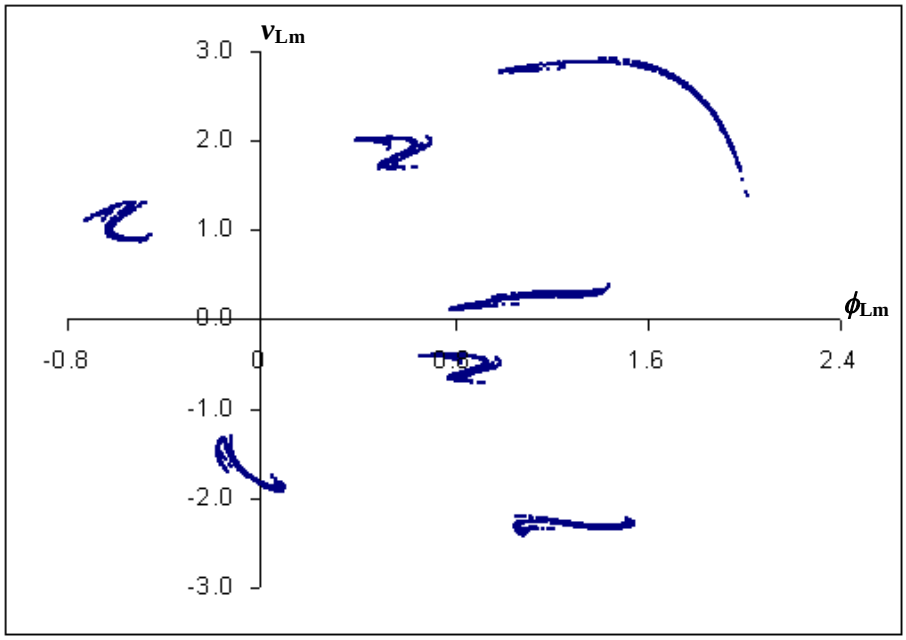

Fig.7.45 Conventional Poincaré map of 7-band attractor at E_{Th} = 1.056216 p.u. in flip segment F of Fig.7.43.

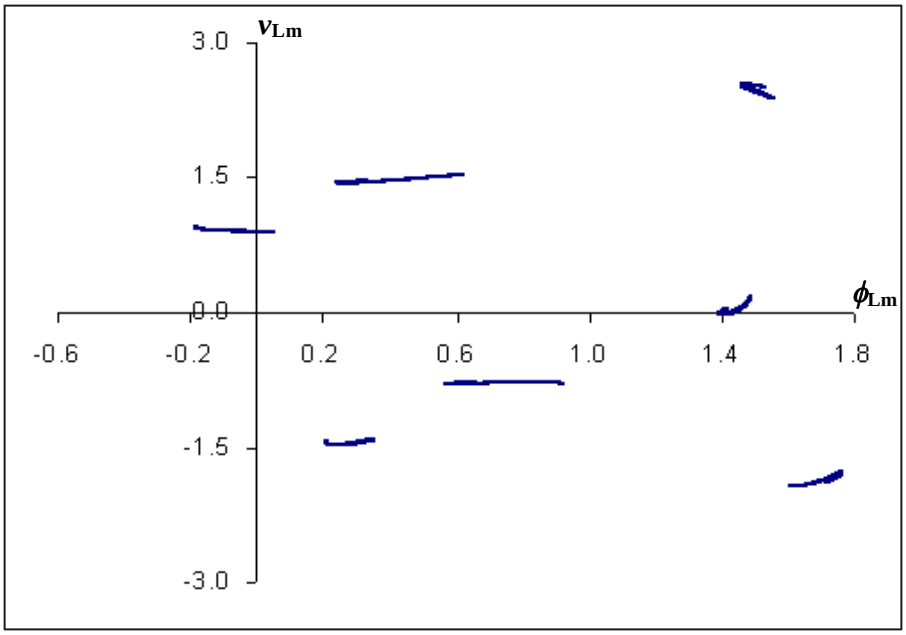

Fig.7.46 Conventional Poincaré map of 7-band attractor at E_{Th} = 1.013607 p.u. in flip segment F of Fig.7.44.

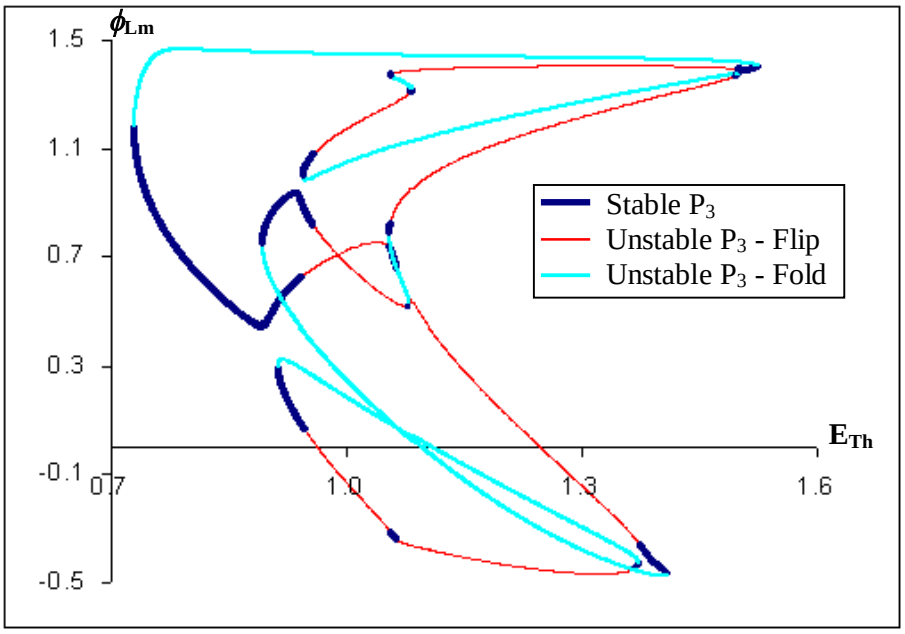

Fig.7.47 Bifurcation diagram of steady state P_3 solution: q = 11, R_m = 600, without arrester, C_{Th} = 0.0616 (Case A.1.4). Initial steady state is obtained from temporal bifurcation diagram, Fig.7.9a.

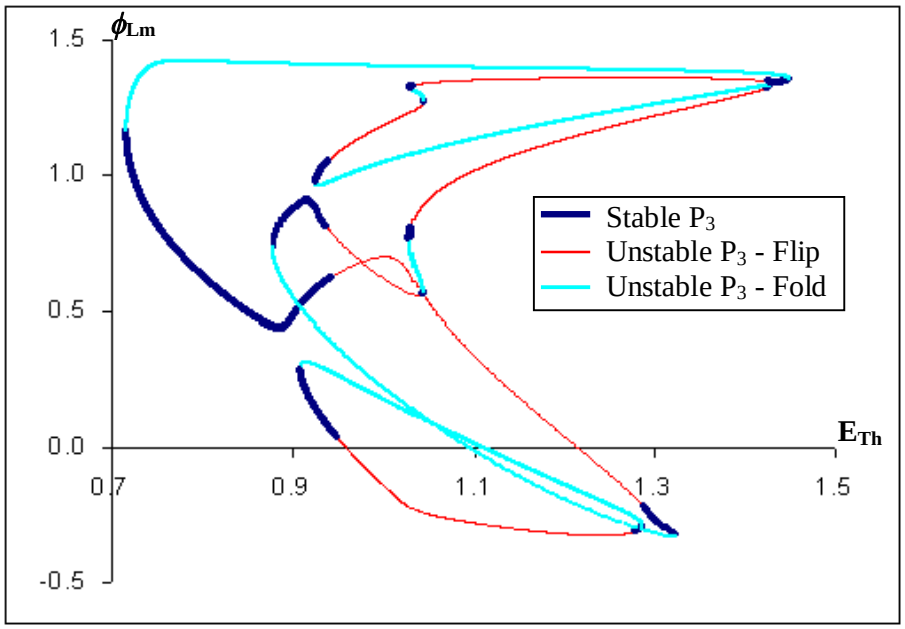

Fig.7.48 Bifurcation diagram of steady state P_3 solution: q = 11, R_m = 600, without arrester, C_{Th} = 0.047 (Case B.1.4). Initial steady state is obtained from temporal bifurcation diagram, Fig.5.7d (Chapter 5).

7.5 SUMMARY

Detailed analysis to explore the effect of MOV arrester, transformer core loss, saturation level and source capacitance on the isolated subharmonic solutions have been reported in this chapter. The salient conclusions are:

- The presence of MOV eliminates the isolated subharmonic ferroresonant solutions for lower saturation index. For higher saturation index, the MOV shrinks the region of stable and unstable subharmonic solutions.
- Banded chaos exists in higher core saturation index case even when the arrester is present.
- The presence of MOV arrester has a significant effect on the range of the subharmonic flip segments.
- Lower transformer core loss increases the range, multiplicity and number of bifurcations of subharmonic solutions.
- Higher core saturation index results in the occurrence of subharmonic solutions at a lower value of bifurcation parameter and increased number of solutions.
- Higher source capacitance widens the range and multiplicity of subharmonic solutions. The effect of source capacitance is predominant in lower core saturation.
- Banded chaos is more likely in the continuum of odd subharmonic solutions.